Surface & Coatings Technology 441 (2022) 128561

Contents lists available at ScienceDirect

Surface & Coatings Technology

journal homepage: www.elsevier.com/locate/surfcoat

Effect of Ti/Si and Ti/TiN/Si interlayers on the structure, properties, and tribological behavior of an a-C film deposited onto a C17200 copper-beryllium alloy

M.D. Santos [a,*], N.K. Fukumasu [b], A.P. Tschiptschin [b], N.B. Lima [c], C.A. Figueroa [d], J.S. Weber [d], R.M. Souza [b], I.F. Machado [b]

[a] State University of Amazonas and Federal Institute of Amazonas, Amazonas, Brazil
[b] Polytechnic School of the University of Sao Paulo, Sao Paulo, Brazil
[c] Center for Material Science and Technology-Nuclear and Energy Research Institute, Sao Paulo, Brazil
[d] University of Caxias do Sul, Caxias do Sul, Brazil

ARTICLE INFO

Keywords:
C17200 copper-beryllium
Coating
DLC
Interlayers
Adhesion strength

ABSTRACT

Reduced hardness and wear resistance may limit SAE C17200 copper-beryllium alloy use in manufacturing applications, such as plunger tips of die casting machines and as cores and inserts for steel dies in injection molding processes. In order to improve the surface properties of Cu—Be alloys, amorphous carbon (a-C) films have been selected since these coatings may show high hardness, low wear rate and low coefficient of friction. However, the adhesion of carbonaceous films on Cu—Be alloys remains a challenge. Two interlayer compositions (Ti/Si and Ti/TiN/Si) were deposited onto Cu—Be disks and silicon wafers to assess amorphous carbon adhesion on substrates made of Cu—Be alloy. The microstructure and topography of the coatings were examined by Field Emission Scanning Electron Microscopy (FESEM) coupled with X-ray dispersive energy spectroscopy (EDS). The chemical composition depth profile was measured by glow discharge optical emission spectroscopy (GDOES), which confirmed distinct coating layers of Ti, Si, a-C (C1 and C2 conditions-pDCMS). A TiN extra layer presence was obtained for the C3 and C4 conditions-pDCMS reactive, confirmed by small angle XRD analysis. Raman scattering spectroscopy showed a higher quantity of sp^3 carbon bonds for C3 and C4 coating conditions compared to C1 and C2. Instrumented indentation tests indicated a higher hardness and reduced elastic modulus for C3 and C4 coating systems, corroborating Raman results, in terms of a higher concentration of sp^3 bonds. Scanning electron microscopy (SEM), atomic force microscopy (AFM), and coherence correlation interferometry (CCI) were used to characterize the coatings' surface features and scratch tracks after the tests. In addition, ramp load scratch tests were conducted to assess coating adhesion to the Cu—Be alloy substrate by measuring critical loads and the coefficient of friction. The highest critical loads to failure (Lc2) and (Lc3) were found for the Ti/TiN/Si interlayer sample (C4 condition), indicating that this interlayer improved the coating contribution to a gradual increase in the hardness and promotion of an enhanced adhesion strength of the a-C coating.

1. Introduction

SAE C17200 copper-beryllium alloy, according to Sousa et al. [1], is widely used in the aeronautical, automotive, electronics and manufacturing industries due to its non-magnetic behavior, corrosion resistance and excellent heat and electrical conduction. Davis [2] indicates typical uses of C17200 alloys as a wide variety of springs, retaining rings, nonsparking safety tools, firing pins, bushings, valves, pumps, shafts, rolling mill parts, electrochemical springs, diaphragms, contact bridges, bolts, screws among others. Cu—Be alloys are also used in the injection molding processes as cores and inserts for steel dies, as shown by Amorim and Weigaertner [3]. Although the Cu—Be alloy is used in several mechanical applications, Yan et al. [4] related that the low hardness and poor wear resistance of Cu—Be alloys are critical, considering the lifespan and failure of components. For instance, one important application of Cu—Be alloy is in plunger tips of die casting

* Corresponding author.
E-mail addresses: mdsantos@uea.edu.br (M.D. Santos), newton.fukumasu@usp.br (N.K. Fukumasu), antschip@usp.br (A.P. Tschiptschin), nblima22@gmail.com (N.B. Lima), carlos.cafiguer@gmail.com (C.A. Figueroa), jsweber@ucs.br (J.S. Weber), robertosouza@usp.br (R.M. Souza), machadoi@usp.br (I.F. Machado).

https://doi.org/10.1016/j.surfcoat.2022.128561
Received 2 March 2022; Received in revised form 13 May 2022; Accepted 18 May 2022
Available online 23 May 2022

machines, as reported by Ahmed and Jailani [5]. In this component, the main wear mode is abrasion, which occurs during the relative movement of plunger tips against the steel sleeves. To capture the abrasive resistance, scratch tests are performed using a diamond ball tip to determine the critical load. Despite being quite severe, this test can reproduce some extreme abrasive conditions that could occur during the application. Seriacopi et al. [6] shows that the abrasive mechanisms are related to properties and microstructures of the materials and can be correlated to scratch test results, which may help to estimate the response of the alloy or coating in different applications.

Regarding surface modification of the Cu—Be alloy, the best results of tribological performance were found using Ti, Ti/TiN, and Cu/Ti coatings processed by a two-step treatment consisting of a magnetron sputtering deposition followed by plasma nitriding, which was reported by Yan et al., Yang et al., Liu et al. and Zhu et al. [4,7–9]. The strong chemical bonds and excellent adhesion to the substrate were directly related to the coating's improved performance. Conversely, an alternative for coating architecture is Diamond-Like Carbon (DLC) films. DLC films present a good combination of mechanical and tribological performance, such as high hardness, high wear resistance, low coefficient of friction, and chemical inertness in several tribosystems, which are attractive and potentially suitable for industrial applications, as suggested by Yatsuzuka et al. [10]. Furthermore, Tyagi et al. [11] indicate that the low deposition temperature allows DLC films to be a competitive coating material. However, the application of DLC films may be limited due to their poor adhesion in different substrates, which is related to the low chemical interaction between the film and the substrate, defects in the film-substrate interface, and the level of compressive stress developed in the film, as reported by Oka et al. and Morshed et al. [12,13].

The adhesion of DLC films to copper substrates is usually very modest, according to Flege et al. [13]. It can be related to the difference between the thermal expansion coefficients (CTE) and the hardness of DLC and Cu—Be alloys, as pointed out by Tonosaki et al. [14]. Age-hardening Cu—Be alloy presents a CTE of 17.8 $\times$ 10^{-6}/K, as presented by Davis [2] and hardness in the range of 3.8 to 4.5 GPa, as displayed by Lomakin et al. [14]. On the other hand, DLC films can present a CTE of 1.5 to 7 $\times$ 10^{-6}/K, as presented by Vetter [15], and a hardness range of 4 GPa to 80 GPa according to Charitidis [16]. Furthermore, low nucleation density, film cracking, and inferior copper-carbon chemical affinity are faced in the coating deposition, as mentioned by Ali et al. [15].

Research works reported by Flege et al., Hongxi et al., Wang et al., Voevodin et al., Maruno and Nishimoto., Lu et al. and Khadem et al. [17–23] describe the use of interlayers to improve DLC adhesion to metallic alloys, mainly when soft substrates are used. The use of a tailored interlayer increases the bond strength between the coating and the substrate and may reduce interfacial stresses, as shown by Holmberg and Matthews [24].

It is worth mentioning that the testing conditions and parameters (load, speed, type of movement, temperature, humidity, and distance) during sliding can modify the tribological performance of different types of DLC, such as amorphous (a-C), tetrahedral (ta-C), nitrogenated amorphous carbon (a-CN) and also their hydrogenated variants (a-C: H and ta-C: H). In addition, mechanisms such as tribo-oxidation, tribo-reactions, graphitization and other phenomena can significantly affect friction and wear rate, as described by Erdemir et al. [25]. and Fukumasu et al. [26]. Likewise, the chemistry of the films or transferred tribofilms and the chemistry/composition of the sliding counter body can influence the friction and wear behavior, according to Scharf et al. [27].

The present work addresses the development of two interlayer compositions (Ti/Si and Ti/TiN/Si) and an a-C functional layer to obtain a hybrid DLC film deposited onto Cu—Be alloy and silicon wafers substrates using Pulsed Direct Current Magnetron Sputtering (pDCMS) and reactive sputtering. Considering that a-C (hydrogen-free DLCs) deposited coatings are rich in sp^2 hybrids and present a relatively low percentage of sp^3 hybrids (less than 20%), an improvement of adhesion and tribological performance is expected due to the tailored graded hardness between the a-C and the metal alloy. The adhesion strength was evaluated using scratch tests at increasing normal load.

2. Experimental procedure

2.1. Substrate

The deposition of the interlayers and the coatings were carried out on an SAE CA17200 copper-beryllium alloy substrate. The substrate's nominal chemical composition (% wt) is 1.89% Be, 0.29% Ni and Cu (balance), according to the manufacturer. Considering atomic percentage, the chemical composition is around 12 at.% Be, 87.5 at.% Cu and 0.5 at.% Ni, which indicates a significant amount of Be. The substrate material was supplied as a rod bar (25.4 mm diameter and 1000 mm length), which was machined to obtain disks of 24 mm in diameter and 8.1 mm in thickness. Si wafers (10x10x0.4 mm^3) substrates were employed to assess the microstructure and thicknesses of the coatings.

2.2. Substrate preparation

The flat surfaces of the Cu—Be alloy disks were obtained following metallographic sample preparation. Samples were ground using silicon carbide sandpaper (180, 200, 360, 600, and 1200 grit) and further polished, utilizing a sequence of diamond solutions: 9, 6, 3, and 1 μm. Monocrystalline Si substrates were obtained from electronic grade wafers and did not require surface preparation.

2.3. Interlayers and DLC functional coating

The low adhesion of the a-C films in copper alloys was reported by Catledge et al. [28] and Lu et al. [21]. According to these authors, it occurs due to the absence of precipitated carbides and the high mismatch interface between the carbon and the copper atoms. In this study, to overcome the copper-beryllium alloy's low hardness and wear resistance, two interlayer compositions (Ti/Si and Ti/TiN/Si) were selected to obtain a functionally graded hardness between the DLC and the soft substrate, as well as to improve adhesion and interfacial diffusivity according to previous studies carried out by Hongxi et al. and Wang et al. [17,18]. The interlayer composition design was employed considering a complex coating concept defined by Voevodin et al. [19], which consists of: i.) an adhesion interlayer deposited on the substrate; ii.) a transition interlayer and iii.) an upper low friction film.

To satisfy the previous concept, titanium was used in all coating conditions because it improves the integrity of interfacial adhesion with the substrate. Furthermore, titanium was selected due to its high diffusivity in copper and silicon, as mentioned by Assali et al. and Fan et al. [29,30]. In addition, Ti has an excellent affinity to carbon, as pointed out by Honjo et al. [31]. To avoid titanium carbide formation, an amorphous silicon layer was deposited to reduce carbon diffusion through the base layer of titanium. The selection of Si was based on its good adhesion strength to carbon-based films, promoted by the low mismatch interface between these two atomic systems and due to bonds that have high covalent energies, as reported by Neuville et al. [32]. The TiN intermediate interlayer was selected to tailor the hardness variation and support the metallic Ti and the amorphous Si. The work by Wang et al. [18] confirms this behavior.

Figs. 1a and b show a schematic illustration of the coating/substrate design. Using polycrystalline titanium and monocrystalline silicon targets, both with a purity of 99.999 wt%, a Pulsed Direct Current Magnetron Sputtering (pDCMS) system was used for the deposition of Ti and Si interlayers. A polycrystalline graphite target (purity of 99.999 wt %) was utilized to produce a hydrogen-free amorphous carbon coating over the tailored interlayer system, aiming to decrease wear and friction

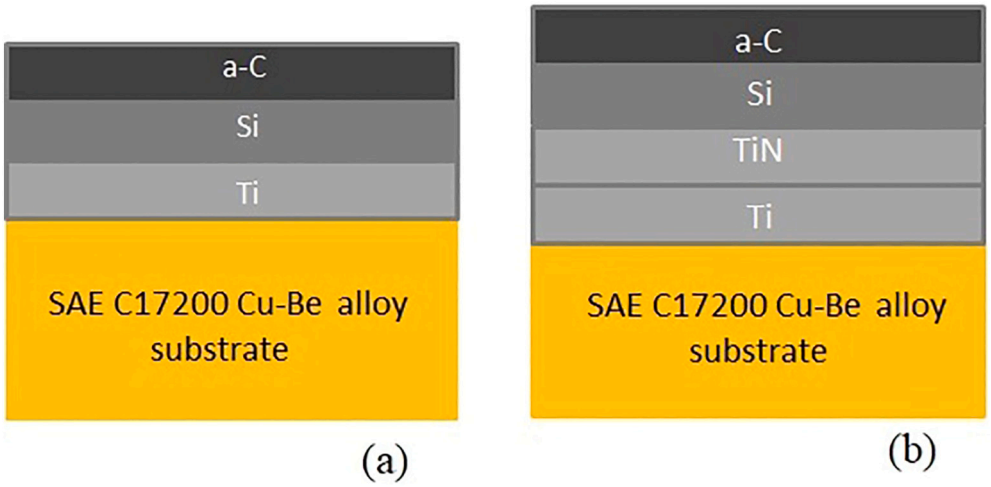

Fig. 1. Schematic illustration of coating layers on top of the substrates: (a) Ti / Si / a-C (SAE C17200 Cu-Be Substrate); (b) Ti / TiN / Si / a-C (SAE C17200 Cu-Be Substrate).

coefficient in tribological conditions. The TiN interlayer was obtained by a reactive deposition process using argon and nitrogen gases and the titanium target.

2.4. Coating deposition processes

Disks of Cu—Be alloy and Si wafers substrates were ultrasonically cleaned in acetone for 10 min before the deposition. The deposition process was carried out in a hybrid PVD reactor and started with an Ar sputtering cleaning step to remove residual contamination on the sample surface. The process parameters for Ar etching considered a gas pressure of 0.02 Torr, a gas flux of 10 sccm, substrate applied power of 150 W using the pulsed DC source with a frequency of 200 kHz, bipolar type and duty cycle of 2 μs, during treatment time of 20 min. Distance between targets and substrates was maintained throughout the deposition process for all coatings conditions and etching. The distance between targets and Cu—Be substrate was 90 mm and for Si wafer was 98 mm. The base pressure prior to the depositions was 0.0001 Torr, and the coating pressure for all depositions was 0.02 Torr. The substrate support was connected to a direct current power source that provided the bias voltage during the deposition of the layers. The magnetron heads were powered by a pulsed DC bipolar source with a frequency of 200 kHz and duty cycle of 2 μs.

The substrates were coated according to coating/substrate design (see Figs. 1 a and b). The (Ti/Si/a-C) coating architecture is displayed in Fig. 1 a and (Ti/TiN/Si/a-C) coating architecture is displayed in Fig. 1 b, with global processing parameters presented in Table 1. For the sake of simplicity, samples were denominated C1 to C4, in which (i) C1 considered a Ti/Si/a-C coating with 0 V bias; (ii) C2 consisted of C1 condition but with −50 V bias; (iii) C3 considered a Ti/TiN/Si/a-C with 0 V bias and TiN deposition for 10 min and (iv) C4 consisted of similar C3 conditions but with a TiN deposition time of 30 min. The uncoated Cu—Be alloy polished disk was denominated as the C0 condition. Table 2 shows the deposition conditions and the number of layers in C1, C2, C3 and C4 coatings. Negative bias values may attract positively charged ions, which bombard the surface of the growing film, resulting in densification mechanisms and re-sputtering of weakly bonded atoms, as explained by Tillmann et al. [33]. Differences between samples C1 to C4 refer to the type of interlayer architecture, the bias voltage applied to the substrate during deposition, and the duration of the deposition of TiN, for the cases where this interlayer was present.

The reactor geometry was cylindrical with three magnetron heads arranged parallel to the axial axis of the chamber, oriented orthogonally to the substrate, as shown in Fig. 2. Moveable support was used to position the substrate below the heads during the deposition process. The substrates were kept onto the support by gravity. The same magnetrons heads of Ti/Si/C were used to deposit C1 to C4 coatings. Therefore, to produce Ti or TiN interlayers the same Ti magnetron head was used. To clean the target before each step in the deposition process, after etching, the magnetron head was kept turned on for 5 min with plasma and argon pressure. The substrate support was positioned out of the magnetron heads during the cleaning. For the deposition of each layer, the substrate support was positioned below a selected magnetron head. Moreover, each head was activated individually, avoiding a simultaneous co-deposition process. Two separate cylinders containing pure N_2 gas and Ar gas, both with 99.9999% purity, were used to feed the chamber. Two independent mass controllers were used to regulate the Ar + N_2 mixture ratio, in which a mixing hub was used to prepare the gases prior to entering the chamber.

Table 1
Deposition process parameters of pDCMS and reactive sputtering.

Parameters/values	Ti interlayer	TiN interlayer	Si interlayer	DLC (a-C) outer layer
Gas	Ar	N_2 + Ar	Ar	Ar
Gas flux/sccm	10	10 + 10	10	10
Target Power/W	250	300	300	300
Substrate Bias/V	0/−50	0	0/−50	0/−50
Deposition time/min	10	10/30	10	90

2.5. Interlayer microstructural characterization

Coatings were deposited onto Si substrates according to the C1, C2, C3, and C4 conditions. Sample cross-sections were obtained by fracture of the Si substrates after being immersed in liquid nitrogen for 10 min and sheared using a stylus. The fractured surface allowed the measurement of coating thickness and microstructure observation using FESEM (FEI-Inspect F50) coupled to an X-ray dispersive energy

Table 2
Deposition parameters and number of layers in the C1, C2, C3 and C4 coatings.

Coating	C1	C2	C3	C4
Number of layers	3	3	4	4
TiN deposition time (min)	0	0	10	30
Bias (V)	0	−50	0	0

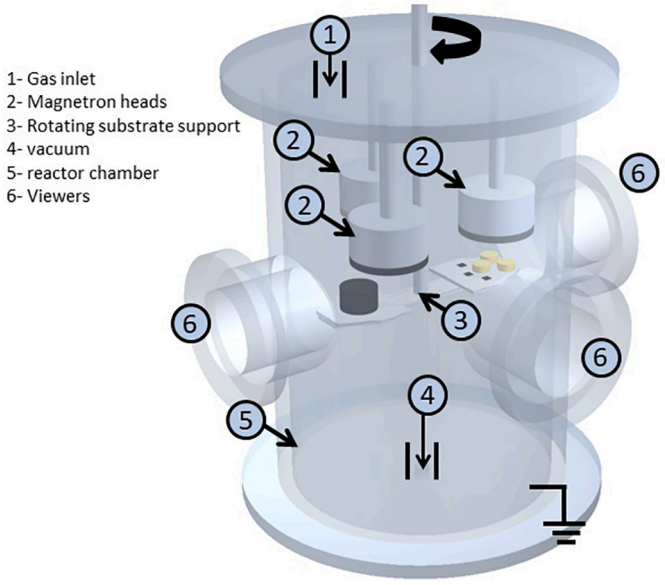

Fig. 2. Schematic illustration of plasma reactor chamber.

spectroscopy (EDS) system. Secondary and backscattered electrons were accelerated at 10 kV to evaluate the microstructural features of the coatings. The coating thicknesses were also determined from cross-sections of the Cu—Be alloy using the FESEM. These samples were mounted and cut using a diamond disk with high precision cut-off. The cross-section surface preparation process followed the usual metallography sample preparation. After polishing and cleaning, the sample was coated with carbon since the bakelite used to embed the samples does not have good electrical conductivity, and the samples were observed using FESEM. The measurement uncertainty was based on standard deviation values of the thicknesses, calculated considering three different measurements of each layer on FESEM images.

2.6. Surface roughness assessment

The atomic force microscopy (AFM) technique, using a Tosca 400 produced by Anton Paar, was applied in tapping mode to assess the surface roughness and images of the top surface topography of the coatings deposited onto Cu—Be alloy. Tests were also carried out to characterize the polished surface of Cu—Be substrate. All the data were processed by Talysurf-Mountains Technology®, which generated two and three-dimensional images and provided the surface amplitude parameters (S_a, S_q, S_p, S_v), according to the ISO 25178 standard.

2.7. X-ray diffraction (XRD)

Diffractograms of the substrate were obtained using an Empyrean 3 system with the powder method, Cu tube, secondary monochromator, Cu kα (λ = 1.542 Å, 2.2 kW) at 45 kV and 40 mA, with a detector variating from 10° - 80° 2θ range in Bragg-Brentano configuration.

Diffractograms of the C1, C2, C3 and C4 coatings were obtained using an X-ray diffractometer (Rigaku Multflex) and CuKα radiation (λ = 1.5418 Å) at 40 kV and 20 mA. Analyses were conducted with a fixed incidence angle of 3°, using grazing angle configuration, with 15° - 82° 2θ range and steps of 0.06° and 8 s/step. The phase identification and structural determination of substrate in C0 condition and samples of C1, C2, C3 and C4 coatings deposited on Cu—Be disk were analyzed using Crystallographica Search-Match software, developed by Oxford Cryosystems Ltd. and comparing the diffractogram of the sample with the PDF2 databases of the ICDD (International Center for Diffraction Data) and ICSD (Inorganic Crystal Structural Database).

2.8. Coating composition depth profile

Qualitative profiles of element composition as a function of depth were obtained using glow discharge optical emission spectroscopy (GDOES). The analyses were conducted in the coated Cu—Be alloy disks, only for C1, C3, and C4 conditions, using a HORIBA GD-Profiler 2. The operating conditions include a discharge pressure of 650 Pa and a power of 60 W. The coherence correlation interferometry (CCI) technique, applied using a Taylor Robson Inc. equipment, allowed the evaluation of the shape and depth of the craters produced by the GDOES technique.

2.9. Raman spectroscopy

A chemical bond analysis was carried out on all Cu—Be coated disks using Raman spectroscopy (Xplora One from Horiba Inc.), employing a 532 nm laser beam with a neutral density optical filter to limit the beam to 10% of the maximum power, thus avoiding degradation of the coatings. The acquisition time of 1 s with two accumulations provided a good signal to noise/ratio. 1200 lines/mm were used in the diffraction grating openings with 100 μm emission slit and 500 μm up take (hole). The nature of the vibration modes of atoms in the DLC films (a-C) was analyzed in terms of resonant excitation. The Raman spectral curves of the deposited a-C films were deconvoluted into two peaks (D and G) and fitted following the Gaussian function, as suggested by Filik et al., Nakao et al., Tai et al. and Wu et al. [34–38]. The Raman spectra of disordered graphite usually show two main modes, the G peak position at 1560 cm^{-1} and the D peak position at 1380 cm^{-1}. These peaks are related to the disordered band (D band) and the graphite band (G band), as pointed out by Ferrari and Robertson [39]. The positions of G and D bands and the integrated intensity ratios (I_D/I_G) are correlated with sp^3/sp^2 chemical hybridization bonds. To estimate the sp^3 content qualitatively, several authors, including Maruno and Nishimoto, Tillmann et al., Nakao et al. and Wu et al. [20,33,35,38], have used the G peak position and the I_D/I_G ratio. However, this correlation is non-linear and depends on process parameters, such as metal doping, hydrogen content, and residual stress level. In order to obtain the average and error of the Gpeak and I_D/I_G ratio, measurements were carried out in triplicate at points close to each other on the surface of each type of coating.

2.10. Mechanical properties

Vickers microhardness of the Cu—Be alloy was evaluated using a Buehler 1600–6306 testing machine, with a load of 0.1 kgf and a dwell time of 10s. Mechanical properties of the coating, including hardness (H), reduced elastic modulus (Er), hardness and reduced elastic modulus ratio (H/Er), and percentage of elastic recovery (% ER), were determined for each sample (Cu—Be alloy disks in C1, C2, C3, and C4 conditions). The percentage of elastic recovery (% ER) was calculated according to the maximum (hmax) and residual (hres) depths obtained from the load-displacement curves, according to the ISO 14577-4:2007 (E) [40] and also described by Maruno and Nishimoto [20].

Load versus displacement curves were obtained using a Bruker Ti950 triboindenter. Indentations were carried out using a Berkovich tip in a low load (maximum 10 mN) configuration module. Calibration curves were performed before testing, according to the triboindenter manufacturer specifications, selecting increasing loads to indent a fused quartz standard. This procedure allowed a calibrated area function in penetration depths ranging from 30 nm to 180 nm. A similar procedure was reported in the literature by Machado et al. [41]. The indentation procedure considered intervals of 5 s, 5 s, and 2 s for loading, holding the load, and unloading the indentation tip, respectively. At least 25 indentations were performed at different regions, and a load range of (0.2–8 mN) was used in the tests. Therefore, multiple indentation loads were carried out to allow analyzing the data in terms of penetration depth compared to coating total thickness in order to separate the influence of substrate hardness, indentation size effect and roughness

properties assessment. The evaluation of the mechanical properties was conducted by the instrumented indentation technique, in which different load versus penetration depth curves are measured in a single indentation procedure. This procedure consists of three steps: (i) increase the normal load applied to the indenter, (ii) hold the maximum load for a few seconds, (iii) release the load, always measuring the position of the indenter tip. After the measurements, those curves are processed using the Oliver & Pharr method [42] to calculate the reduced elastic modulus and the hardness of the material.

2.11. Scratch tests

Instrumented scratch tests were carried out in a Bruker UMT-2 tribometer, with the load being linearly increased from the preload of 1 N to 20 N in 240 s with a scratch distance of 5 mm, following directives from ASTM C1624–05 standard [43]. The tests were carried out at room temperature and humidity (%) of 55 ± 10. The critical loads of Lc1, Lc2, and Lc3 for the coatings microcracking and delamination were determined. According to ASTM C1624–05 standard, a Rockwell C indenter - diamond cone with an apex angle of 120° and a 200 μm tip radius should be used. This standard correlates different failure modes (cohesive, adhesive and delamination) to Lc1, Lc2, and Lc3 critical loads, determined based on the variations of the frictional force and acoustic emission signals following the procedures carried out by Wu et al. [38]. The surface topography and the scratched film failure were observed in a JEOL JSM-6010LA scanning electron microscope (SEM) with EDS analysis, using a secondary electron detector with different magnifications under a 10 kV acceleration voltage. At the end of the scratch track (maximum normal load), the EDS images were processed using Image J software to investigate the arising of the Cu—Be alloy substrate. The coherence correlation interferometry (CCI) was also used to assess the scratch depths and the pile-ups along with the scratch marks.

3. Results and discussion

3.1. Cross-section microstructure and thickness of the coatings

Figs. 3 a to h present the cross-sectional microstructure of Ti/Si/a-C and Ti/TiN/Si/a-C coatings deposited onto the Si wafers. Table 3 shows the thickness values of each layer deposited on Si wafer and Cu—Be alloy substrates.

Figs. 3a and b refer to the C1 and C2 samples, which resemble columnar structure and epitaxial growth of the films. In this regard, the properties of C1 and C2 could be modified with a different bias. Similar results with graphite-like amorphous carbon film were reported by Wang et al. and Wang et al. [44,45]. According to previous literature, low hardness and adhesion may be correlated with the weak density and energy present in columnar structures. Furthermore, columnar boundaries are a potential source of failure because they facilitate the crack initiation and propagation, which are detrimental to film wear behavior, as reported elsewhere by Chen et al. and Shaha et al. [46,47]

For C3 and C4 samples, a TiN interlayer was introduced in the coating architecture. The TiN interlayer was smaller in the C3 than in the C4 sample (see Table 3). A thinner TiN layer was expected for the C3 sample, as the deposition time was shorter than C4. The TiN deposition time also influenced the C3 and C4 coating microstructures. The C3 sample (Fig. 3c) does not show evidence of a columnar morphology, revealing equiaxial grains. However, TiN layer thickness, which is between the Ti and Si layers, was not accurately determined in C3 coating on Si wafer even using 100.000 magnification (FESEM). Nevertheless, TiN interlayer in the C3 condition deposited on Cu—Be alloy was observed, and a thickness of 86 nm was found, as shown in Table 3.

In the C4 condition, the transition region of densely packed fibrous grains in the coating was observed along with the film thickness, as reported by Thornton [48]. Fig. 3 d also displays similarities with columnar structures, mainly for Ti and TiN layers. Comparable microstructures were also observed by Voevodin et al. [19]. According to Petrov et al. [49], the key to explain the non-uniform microstructure of grains is the competitive growth at the interface (exhibited by V-shaped grains) since grains with different crystallographic orientations lead to different diffusion coefficients and, consequently, other residence times for adatoms are found.

Table 3 also shows the thickness of each layer of deposited coating conditions on both Si and Cu—Be alloy substrates. Thicker total thicknesses were observed in samples deposited onto Cu—Be disks than those deposited onto the silicon substrate. Therefore, the total thickness of the coating deposited over the Si wafer was lower than Cu—Be samples, especially on C1 and C2 samples. Also, conditions C3 and C4 presented smaller Si and a-C layer thicknesses compared to the C1 condition. This feature was not considered during the deposition process and it will be the subject of upcoming work.

3.2. Surface roughness

Table 4 shows selected roughness parameters of the surface topography measured on the uncoated polished disk C0 and C1 to C4 deposition conditions samples. The polished surface of the uncoated Cu—Be alloy disk shows low roughness (see Table 4), and results were similar to those reported in the literature by Jiang et al., Svanh et al. and Bernardes et al. [50–52]. Therefore, the preparation of the samples was considered suitable for the coating process.

Nevertheless, an increase in all roughness parameters of the C1 and C2 coated samples was observed compared to the uncoated polished substrate data. A similar increase was reported by Hofmann et al. [53] and can be explained based on the different characteristics of the coated samples. The roughness of the a-C coating obtained with C1 and C2 conditions replicated the roughness of the Ti interlayer, developed from the columnar morphology shown in Figs. 3a and b. The top view of C1 and C2 samples, acquired by AFM, is shown in Figs. 4b and c and reveals semi-spheres-like colonies on the surface. Notably, the C2 sample presented a lower surface roughness than the C1 coated sample. Larger semi-spheres are found in the C1 sample. The difference is probably a result of the -50 V bias applied during the preparation of sample C2. As reported by Tillman et al. and Tillmann et al. [33,54], the more significant negative bias generates a larger flux and energetic bombardment of ions, promoting a more uniform and compact structure on the film surface.

The C3 condition, for which equiaxial grains were observed (Fig. 3c), replicated a uniform distribution of fine semi-spheres over the film's surface (Fig. 4d). In this case, the a-C displayed lower surface roughness than C1 and C2 conditions, as shown in Table 4.

Finally, the C4 condition resulted in excellent surface roughness and it can be related to microstructure and V shaped type of grains. A more compact and denser structure was observed, but it was challenging to observe grain boundaries (Fig. 4e) as reported in the literature by Kluth et al. [55] and Thornton [56]. The film growth probably resulted in the material filling the valleys of both C3 and C4 samples, and, consequently, a decrease in roughness parameters was observed.

3.3. XRD

Figs. 5a and b show the X-ray diffraction patterns of substrate and coatings deposited with C1 to C4 conditions. The Cu cubic crystalline structure, (ICSD) 043493, and PDF number (#01–089-2838) were present in the substrate and the peaks corresponding to plane (111) (200) and (220) were found. In the coated samples, the Cu cubic crystalline structure, ICSD (64699), and PDF number (#000–04-0836), was observed in all samples, reflecting information from the substrate with similar peaks (111), (200), and (220). The Beryllium copper (BeCu) cubic crystalline structure, PDF number (#03–065-3195) was also present in the substrate. The Ti or alpha-titanium phase with hexagonal crystal structure was also identified in all coating conditions. Peaks at

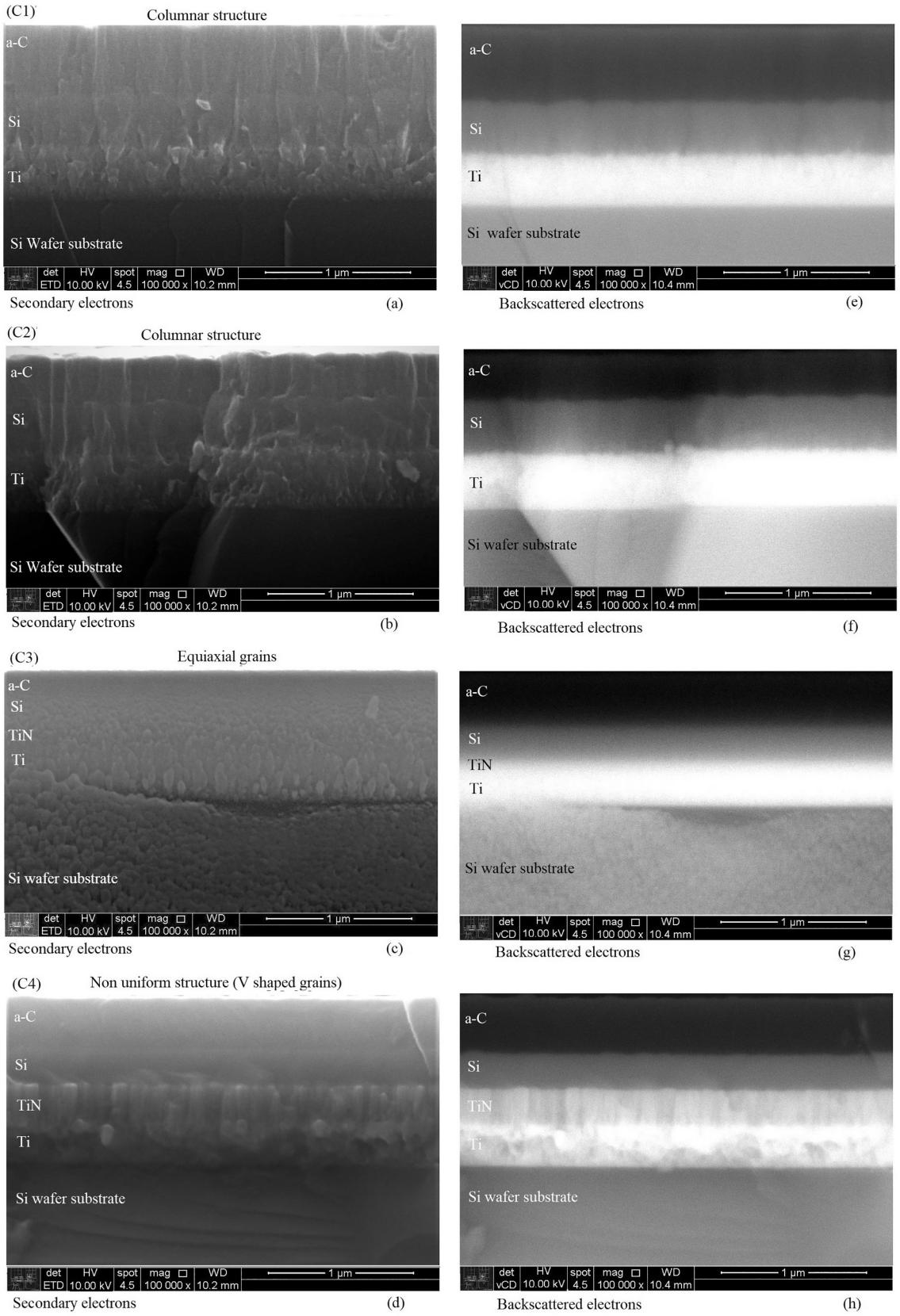

Fig. 3. Fractured cross section micrographs of the coatings deposited on Si substrate. FESEM, secondary electron (SEI) and back-scatter (BEC) detectors: a) (C1) SEI; b) (C2) SEI; c) (C3) SEI; d) (C4) SEI; e) (C1) BEC; f) (C2) BEC; g) (C3) BEC; h) (C4) BEC.

Table 3
Thickness of each layer deposited on Si wafer and Cu—Be alloy substrates determined through microstructure observation – FESEM, backscattered electrons, 10 kV.

Coatings/ thickness	Ti interlayer (nm)	TiN interlayer (nm)	Si interlayer (nm)	a-C film (nm)	Total thickness (nm)
C1 on Si Wafer	346 ± 4	–	372 ± 10	475 ± 27	1194 ± 49
C1 on Cu—Be disk	594 ± 43	–	644 ± 15	998 ± 55	2236 ± 33
C2 on Si Wafer	407 ± 31	–	397 ± 17	296 ± 25	1100 ± 9
C2 on Cu—Be disk	565 ± 16	–	610 ± 40	457 ± 37	1634 ± 20
C3 on Si Wafer	258 ± 52[a]	–	271 ± 20	357 ± 6	886 ± 34
C3 on Cu—Be disk	318 ± 4.9	86 ± 1	258 ± 10	448 ± 7	1110 ± 21
C4 on Si Wafer	269 ± 10	232 ± 17	239 ± 10	356 ± 9	1096 ± 42
C4 on Cu—Be disk	300 ± 4	259 ± 4	265 ± 20	422 ± 4	1247 ± 24

[a] Ti interlayer is overestimated since TiN interlayer is thin and it was not observed in the C3 condition. The nitrogen atomic mass is lower than Ti. Therefore, identifying the interface between Ti and TiN was not possible.

Table 4
Quantitative parameters of sample surface topography evaluation – Roughness.

Coating/ roughness	Average height, Sa (nm)	Mean root square height, Sq (nm)	Maximum height, Sp (nm)	Maximum depth, Sv (nm)
Topography C0 uncoated Cu—Be disk	2 ± 1	3 ± 1	21 ± 1	11 ± 1
Topography C1 on Si wafer	9 ± 1	12 ± 1	69 ± 7	49 ± 2
Topography C1 on Cu—Be disk	11 ± 1	15 ± 2	77 ± 5	82 ± 5
Topography C2 on Si Wafer	6 ± 1	8 ± 1	32 ± 4	33 ± 3
Topography C2 on Cu—Be disk	10 ± 1	13 ± 1	46 ± 9	49 ± 5
Topography C3 on Si Wafer	2 ± 1	2 ± 1	8 ± 1	4 ± 1
Topography C3 on Cu—Be disk	3 ± 1	4 ± 1	19 ± 1	13 ± 1
Topography C4 on Si Wafer	3 ± 1	4 ± 1	20 ± 1	14 ± 1
Topography C4 on Cu—Be disk	4 ± 1	5 ± 1	19 ± 1	14 ± 1

(100), (002) and (101) of titanium crystallographic planes were identified, based on ICSD (076265) and PDF number (#000–89-5009).

The titanium nitride (TiN) – osbornite – has a cubic crystal structure, and it was detected only for condition C4 (ICSD (064909) and PDF number (#000–87-0633). Peaks corresponding to (111), (200), and (220) were identified. According to Saikia et al. [57], it is worth noting that most TiN coatings exhibit a preferential crystallographic orientation, which affects the mechanical behavior of the coatings. In this study, the preferential orientation of the TiN was determined based on the position of the (111) peak, which according to the ICSD data, presents the largest intensity at diffraction angle 2θ equal to 36.6°. However, to find the inclination of this plane concerning the surface of the sample, the angle θ of 18.8° was subtracted from the angle of incidence (3°), resulting in approximately 15.8°. From previous results and connecting interplanar angle in cubic crystal structure between planes, according to Cullity [58], the nearest plane of the preferred orientation was determined as (221).

For condition C3, the TiN interlayer is relatively thin (see Table 3) and not detected using X-ray diffraction due to the low intensity diffracted X-rays coming from this layer. In addition, C3 sample presented a high intensity Cu peak at (220), compared to (111), contrasting with other samples. This result may be related to sample preparation since they were taken from different regions of the same round bar, in which different preferential orientations along the bar may occur.

Finally, Si and a-C deposited were expected to be amorphous under all coating conditions, producing no diffraction patterns under regular measurements.

3.4. Coating composition depth profile

GDOES analyses were conducted to qualitatively evaluate the coating chemical composition of C1, C3, and C4 samples. C2 sample was not assessed because previous damage caused by scratch and wear tests have affected the results.

Fig. 6 shows complementary analysis carried out as follows. Figs. 6a, d, and g display the region assessed during GDOES analysis (sputtered craters), in which a circle of 4000 μm in diameter can be observed. Black arrows indicate the regions sputtered by the GDOES plasma. The red arrows indicate the surroundings of the region assessed (coating deposited). Figs. 6b, e, and h reveal the depth profile of the area analyzed by GDOES. Finally, Figs. 6c, f, and i show the qualitative results of the elemental chemical composition obtained by GDOES as a function of depth for each type of coating. The dashed green vertical lines delimit the regions of the interfaces between the Cu—Be alloy substrate and the interlayers and between the interlayers and the a-C outermost film.

Fig. 6c displays C, Si, Ti, Cu, and N, results for the C1 condition. The nitrogen signal presents a decrease in the intensity with depth profile in the region of the interlayers. The analysis in the C1 sample was in agreement with the deposition process since N_2 gas was not used during this deposition process. Fig. 6c depicts the N and C signal up to approximately 1.0 μm in-depth profile. It may result from C1 sample contamination of a-C film surface with atmospheric air, rich in nitrogen, or a background signal.

Figs. 6 f and i display signals for C, Si, Ti, N and Cu. Figs. 6f and i also indicate the existence of N signal that suggests TiN formation since N signal was concomitant with Ti signal. For the C3 condition, the nitrogen maximum intensity signal peak is 0.06 at a depth of 0.6 μm. In the depth of 0.4 and 0.6 μm, the a-C functional layer decreases, and Ti increases. On the other hand, in C3, the lowest N signal intensity was detected in the largest signal region of the a-C layer between the depths of 0 and 0.4 μm. Similar results can also be observed for C4 sample. However, it presented the highest N intensity, probably due to the longer deposition time in N_2 gas in the pDCMS reactive process, which determines a denser TIN phase. Indeed, XRD patterns in Fig. 5b shows a diffracted peak at 36.6° for sample C4 that is related to a dense plane (111), in terms of atoms, for TiN. These experimental results of GDOES are additional evidence of the existence of the TiN interlayer in C3 and C4 coatings and confirm the results of FESEM thickness measurements (see Fig. 3) onto Cu—Be disks. It is worth mentioning that during GDOES analysis, the depth resolution depends on the variation of sputtering rate across the crater, as described by Shimizu et al. [59]. Florian et al. [60] also described that the intensities at the precise wavelengths result from each element's emission in the glow-discharge plasma at a given moment. Therefore, the transformation of the measured intensities to quantitative concentrations of each component depends on sputtering rate factors or specific emission characteristics. In addition, the surface roughness may also affect the spatial resolution.

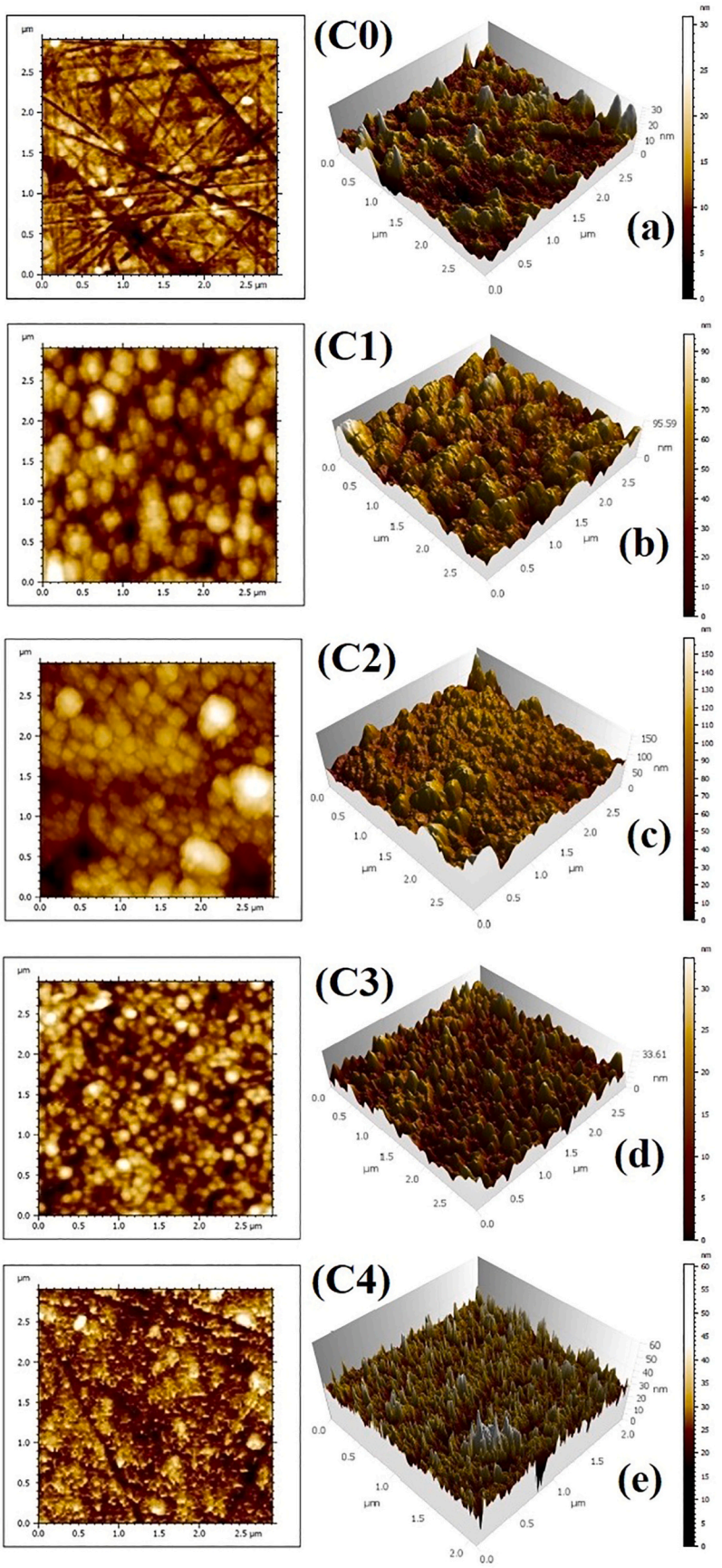

Fig. 4. Top view (topography) and 3D view of (a) uncoated substrate (Cu-Be alloy) and coated surfaces on the Cu-Be alloy disk samples: (b) C1 coating; (c) C2 coating; (d) C3 coating; (e) C4 coating. Atomic Force Microscopy (AFM).

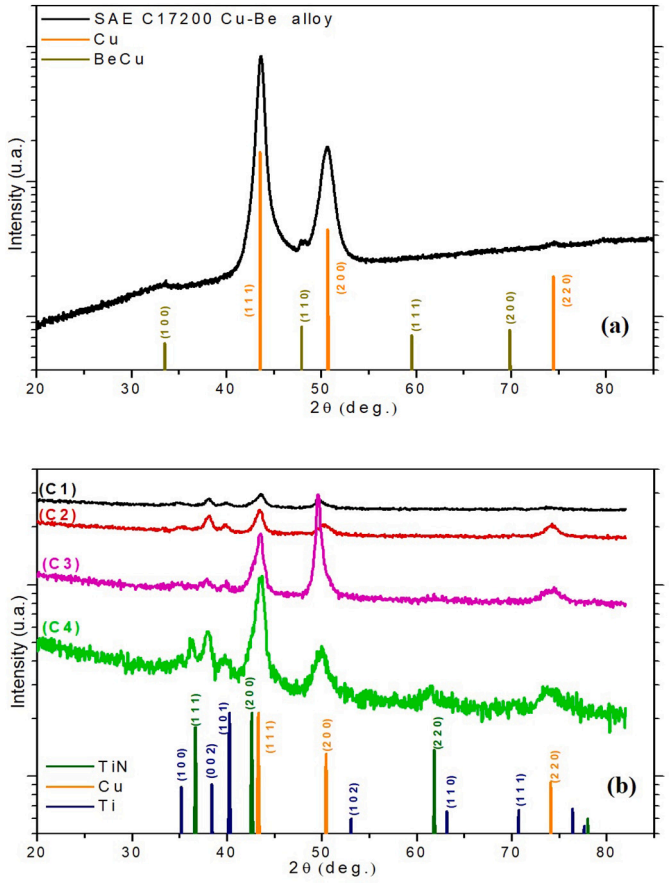

Fig. 5. X-ray diffraction patterns: (a) Cu-Be alloy substrate and (b) C1 to C4 coatings deposited onto Cu-Be alloy disks.

3.5. Raman spectroscopy

Fig. 7 shows Raman's original spectra, fitted curves, and the position of peaks (D and G) of the a-C films. Fig. 8 shows the I_D/I_G intensity ratio and the value of the G peak position for the same coatings. A comparison between C1 and C2 Raman results reveals that the carbon films exhibited a graphite-like carbon (GLC) microstructure with a predominant sp^2 hybridized carbon bond, according to Wang et al. [44]. A decrease in the G peak position (1573.8 ± 0.3 to 1568.4 ± 2.8 cm^{-1}) indicates a slight reduction in the content of sp^2 bond. Similar results were reported by Wang et al. [45], which is related to applying a substrate bias of −50 V for condition C2. Therefore, both coatings present G peak position values higher than 1560 cm^{-1}, suggesting the formation of predominant carbon sp^2 phase (clusters) in the amorphous carbon films, as reported in previous works by Ferrari and Robertson, Wang et al., Wang et al., Chen et al. and Huang et al. [39,44–46,61]. Fig. 8 also shows a G peak position reduction and an increase in the I_D/I_G ratio when TiN layer was deposited. In particular, C4 sample a-C film resulted in a lower G peak position (1546.1 ± 3.3 cm^{-1}) compared to condition C3 (1550.6 ± 4.8 cm^{-1}). This difference in the G peak position may be attributed to the growth of a-C film on top of TiN instead of Ti layer, which promoted a mechanical - chemical interaction. It is important to highlight that C4 presented a significant content of TiN layer that was observed in SEM and XRD results. Conversely, the TiN layer of C3 coating condition was very thin (observed only by FESEM in the deposition on Cu—Be), resulting in an intermediate condition for the G peak position.

It is worth noting that Ferrari [62] indicates that the G peak position and I_D/I_G ratio ranges of carbon films found in this work may be classified as hydrogen-free a-C in stage 2 of amorphization trajectory, with sp^3 content ranging between 1% to 10% for the C1 and C2 conditions, while sp^3 content would be between 10% to 20% for the C3 and C4 conditions.

3.6. Mechanical properties of coatings on Cu—Be alloy substrate

Measurements of microhardness in the Cu—Be alloy bar resulted in 380 ± 13 HV for the longitudinal section and 430 ± 13 HV in the cross-section of the samples.

Table 5 displays the values of the mechanical properties of samples deposited on both Cu-Be alloy and Si wafer substrates, calculated based on nanoindentation data for C1 to C4 coating conditions. The maximum depth (hmax) was obtained considering a normal load of 2 mN for C1 and C2 conditions and a load of 8 mN for C3 and C4.

Fig. 9 shows typical load-displacement curves for the analyzed coatings deposited on Cu—Be substrate. No incidents (pop-ins or pop-outs) were observed on the curves. These measurements indicate that C3 and C4 coating conditions could withstand higher normal loads compared to conditions C1 and C2 for similar penetration depths.

The influence of the bias voltage of −50 V (C2 condition) was observed as a slight increase in the hardness and reduced elastic modulus compared to the C1 coating. Nevertheless, both C1 and C2 coatings presented low hardness values and reduced elastic modulus, as shown in Table 5, considering the substrates of Cu—Be alloy and Si wafer. The low hardness for C1 and C2 may be related to the growth of the a-C film on top of Ti alpha layer (see DRX results), which has a low hardness value (between 3 and 4 GPa) and was also observed by Song et al. [63] and Wang et al. [44]. Likewise, these reduced mechanical properties were compatible with Raman results for the C1 and C2 coatings, in which high sp^2 content was found, indicating the presence of graphite structures. According to Valencia et al. [64], the low hardness and reduced elastic modulus are due to the low concentration of sp^3. Kulikovsky et al. [65] also obtained a-C film hardness below 5 GPa. These results were related to the increase in Ar pressure leading to a decrease in microhardness and intrinsic stress and, consequently, an enlargement in the intensity of both the D and G band due to the rise of sp^2 bonds of carbon. D. Martínez-Martínez et al. [66] reported a hardness of approximately 3.7 GPa in a structure of TiC/a-C nanocomposite coatings, with a-C phase of 96.1% and 3.9% of Ti content. These compositions cause an abrupt decrease in the hardness due to the grain separation becoming too big, and the soft a-C dominates the general behavior.

In this study, the highest hardness and elastic modulus found in conditions C3 and C4 in both substrates (see Table 5) are related to the functional film support layer made of TiN. The Ti/TiN/Si/a-C configuration system promoted higher sp^3 content, indicated by the decreased G peak position (see Fig. 8) of Raman results. The sp^3 bond content depends on the energy of the carbon and ions that reach the surface of the growing film, which are directly related to deposition parameters and coating composition produced by the magnetron sputtering process. The hardness is slightly higher in the C3 coating (see Table 5) than C4 condition.

Figs. 10a and b show the hardness and reduced elastic modulus for all coating conditions as a function of indenter penetration depth. This figure indicates a low dispersion of hardness and reduced elastic modulus data for each sample, even when indentation depths reached about 20% of coatings' total thickness.

Fig. 11 depicts the values of the plasticity index (H/E_r) and (H^3/E_r^2). The hardness ratio to reduced elastic modulus (H/E_r) effectively indicates a surface capability to resist mechanical damage and failure. Cubed hardness over squared reduced elastic modulus ratio (H^3/E_r^2) expresses how likely the film is plastically deformed and indicates the toughness as explained by Charitidis [16].

The higher plasticity index (H/Er) in C3 and C4 samples indicates elastic recovery and the ability to withstand higher external loads. According to Leyland and Matthews [67] and Liu et al. [37], the plasticity

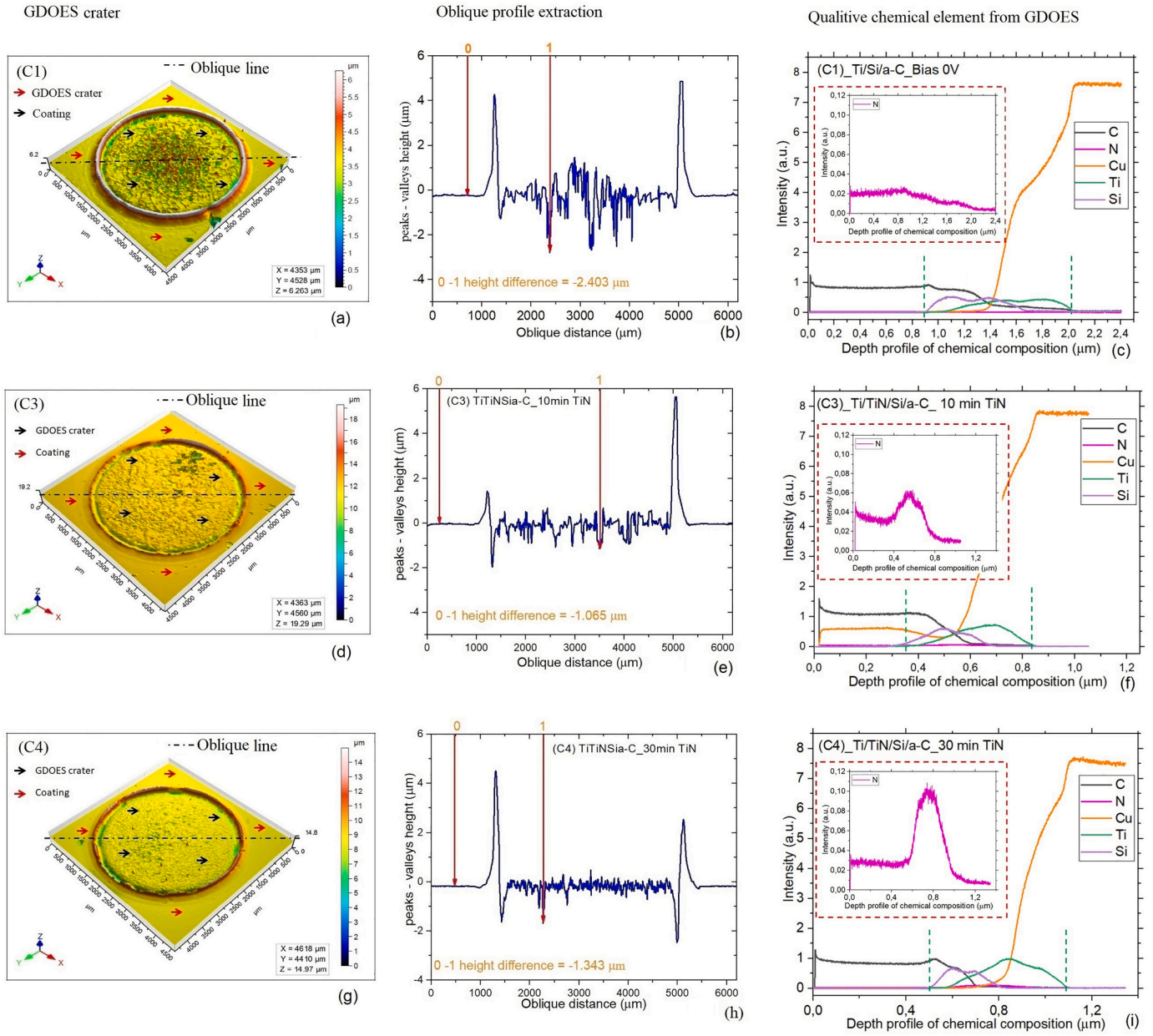

Fig. 6. GDOES crater, oblique profile extraction and qualitative profile images of the chemical elements and the crater resulting from the GDOES sputtering process as a function of the coatings depths on the copper-beryllium alloy disks: (a), (d) and (g) 3D optical profilometry for C1, C3 and C4 GDOES samples crater, respectively; (b), (e) and (h) Oblique profile extraction for C1, C3 and C4 samples, respectively; (c), (f) and (i) qualitative chemical analysis of C1, C3 and C4 samples, respectively.

index is usually a good wear resistance indicator. It is worth mentioning that the increase in the hardness of the coating implies an improvement in resistance to plastic deformation, but fracture toughness may be reduced. The ratio (H^3/Er^2), displayed on the right axis of Fig. 11, indicates an increased C3 and C4 coatings capacity to support overall plastic deformation compared to C1 and C2.

3.7. Scratch tests

Figs. 12a and b show adhesive coating failures for samples prepared according to C1 and C2 conditions. Both samples presented coating detachment, revealing the substrate underneath. A more detailed observation of the results shown in Figs. 12a and b reveal the predominant failure mode was wedge spallation, as explained by Bull [68]. The failure occurs at the onset of the scratch track, indicating low adhesion and, consequently, quick adhesive failure of the coating. The continued forward motion of the indenter drives spalling in the direction of the scratch track and wedges of the adjacent coating under the segment bounded by compressive shear crack, causing decohesion of the interface. The predominant failure mode for conditions C3 and C4 was buckling, as revealed in Figs. 12c and d. Those failures occur as curved tracks extend to the edge or beyond the scratch track. At the end of the scratch track, see Figs. 12c and d, spallation was associated with buckle failures, which denotes adhesive failure.

Figs. 13a to d show the scratch test results (the tangential, normal force, and coefficient of friction data alongside the scratch distance) for C1 to C4 samples. The identified critical loads (Lc1, Lc2, and Lc3) and composite images of the scratch track with semi-quantitative chemical analysis (EDS) are also displayed.

Comparing the scratch curves of the C1 and C2 conditions shown in

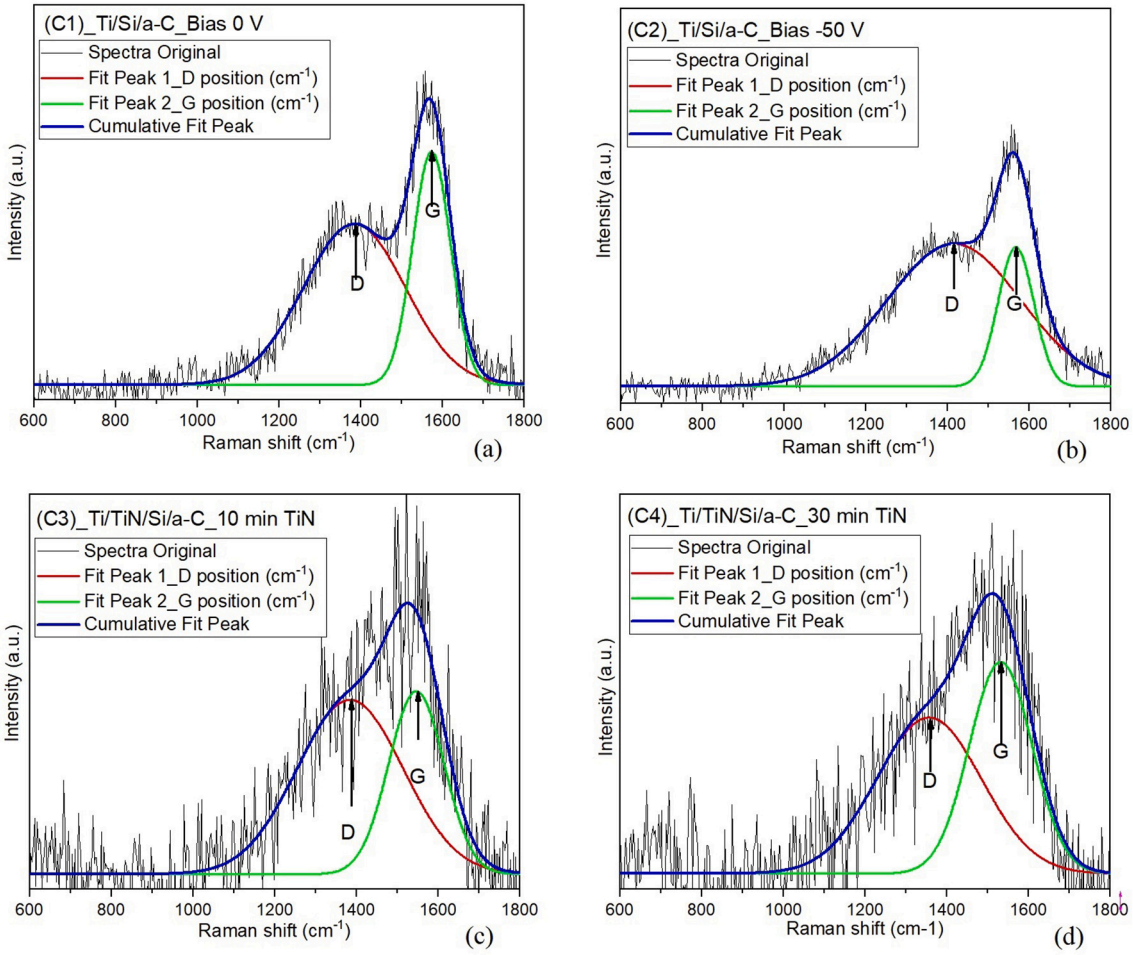

Fig. 7. Raman spectra and fitted curves of a-C films measured at 532 nm excitation wavelength and deposited on the copper-beryllium alloy disks: (a) C1 coating; (b) C2 coating; (c) C3 coating; (d) C4 coating.

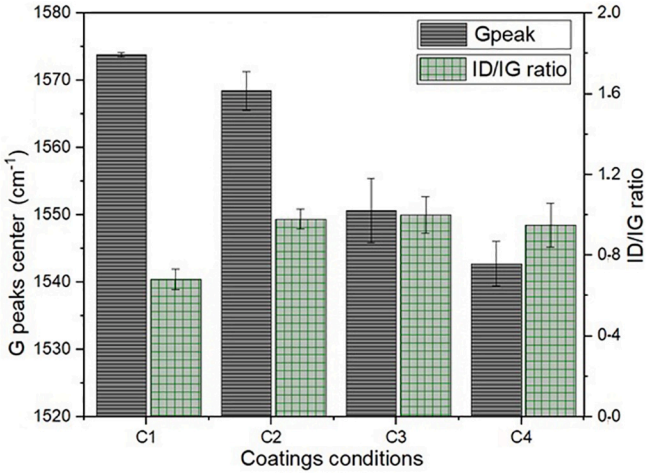

Fig. 8. Correlation between G peak position and ID/IG of Raman spectra parameters after fitted curves.

Table 5
Hardness (H), reduced elastic module (Er), maximum depth (hmax), residual depth (hres), and elastic recovery (ER%) of C1 to C4 coatings deposited on Cu—Be alloy and Si wafer substrates.

Coatings/ properties	Normal load (mN)	Er (GPa)	H (GPa)	hmax (nm)	hres (nm)	ER (%)
C1 on Si wafer	1.0 to 5.8	45 ± 9	2.7 ± 0.5	237 ± 66	36 ± 6	84
C1 on Cu—Be disk	0.2 to 2.0	28 ± 4	2.8 ± 0.6	196 ± 8	54 ± 5	72
C2 on Si wafer	1.0 to 5.8	61 ± 10	3.3 ± 0.2	205 ± 47	41 ± 18	80
C2 on Cu—Be disk	0.2 to 2.0	36 ± 1	3.4 ± 0.5	170 ± 4	52 ± 3	69
C3 on Si wafer	1.0 to 5.8	85 ± 7	12.0 ± 0.3	128 ± 39	31 ± 11	76
C3 on Cu—Be disk	0.8 to 8.0	134 ± 6	16.0 ± 1.3	176 ± 1	62 ± 3	65
C4 on Si wafer	1.0 to 5.8	124 ± 7	14.3 ± 1.3	108 ± 31	34 ± 13	69
C4 on Cu—Be disk	0.8 to 8.0	137 ± 1	15.2 ± 0.8	172 ± 3	61 ± 1	64

Figs. 13a and b, whose depositions differ only in the substrate bias voltage (from 0 to −50 V), the cracks start to propagate brittle, causing complete delamination, and the substrate was exposed. In this way, the critical load is denominated as Lc_3, as suggested by Tillmannn et al. [69]. For the C1 condition, Lc3 was 6.4 N, and for the C2 condition, 5.8 N; thus, the applied bias voltage slightly reduced interfacial adhesion for the C2. According to Tillman et al. [54], the bias voltage influences the microstructure and mechanical properties and the adhesion of amorphous carbon films deposited by magnetron sputtering. However, the higher thickness in C1 (2236.5 nm) than C2 (1634.8 nm) may also have contributed to a higher strength adhesion for C1. Therefore, the combination of lower adhesion, more significant bias and thinner thickness

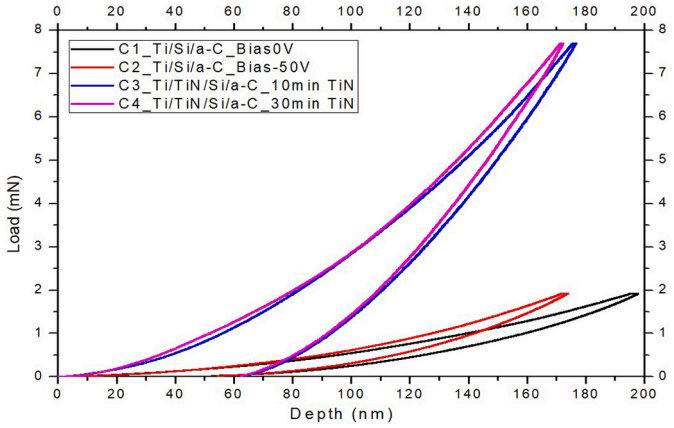

Fig. 9. Load-penetration depth curves results of instrumented indentation applied to evaluate coatings in conditions C1, C2, C3 and C4 deposited on Cu-Be alloy disks.

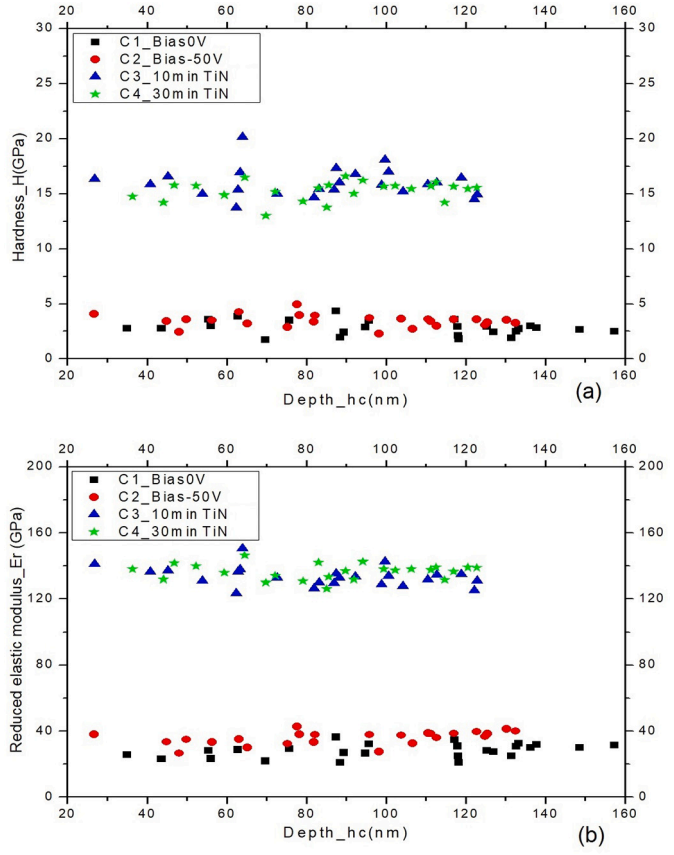

Fig. 10. Results of coating mechanical properties deposited on Cu-Be alloy disks: (a) Hardness (GPa); (b) Reduced elastic modulus (GPa).

in the C2 coating condition explains why the adhesive failure occurred at a more downward scratch distance than C1 coating. Figs. 13a and b also displays the images processed by Image J software applied to EDS mappings. It was possible to notice that the C1 and C2 coatings showed an extensive exposition of the copper substrate at the end of the scratch track. The lower coefficient of friction (COF) of 0.12 for C1 than 0.14 for C2 can also be related to the thicker coating in the C1 condition. Therefore, C2 lower thickness would promote the higher deformation of the coating/substrate system. In addition, Ti/Si/a-C coating system for C1 and C2 samples presented a lower COF than Ti/TiN/Si/a-C for C3 and

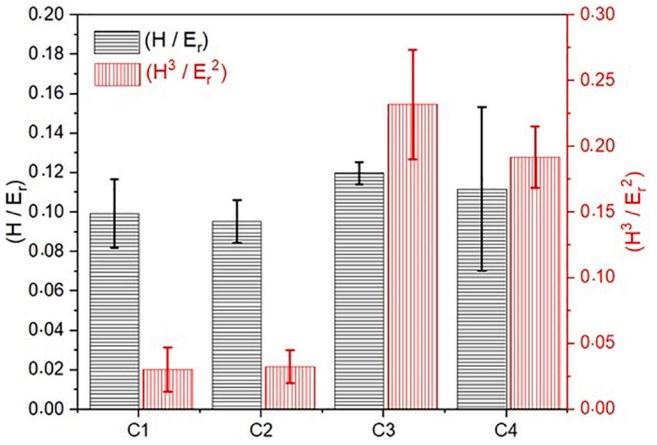

Fig. 11. (H / Er) and (H3 / Er2) for coatings on Cu-Be alloy substrate.

C4 samples.

Figs. 13c and d show results of scratch tests carried out on C3 and C4 specimens, indicating a considerable increase in Lc3 critical loads (17.1 N for C3 and 18.2 N for C4) compared to C1 and C2. Therefore, the effect of TiN layer in a-C functional layer was beneficial to the adhesive strength of the coating. According to Godinho et al. [70] and Liu et al. [71], the multilayer gradient acts as a buffer and considerably improves the mechanical properties, tribological behavior, and adhesion of the a-C films. Furthermore, observing the composite images of the C3 and C4 samples and considering the EDS mapping, it is possible to notice a small area of substrate exposure at the end of the scratch track.

Figs. 13c and d also show the end of scratch regions in both C3 and C4 samples, corresponding to the complete delamination of a-C. The TiN layer improved the mechanical support at the highest normal load. The curves also presented an increase in the tangential forces in similar regions for C3 and C4 sample conditions. The magenta line (COF) indicates the apparent coefficient of friction between the diamond indenter and the coatings in Fig. 13. COF value was around 0.10 below Lc1 regions for C3 and C4 samples. However, at the end of the scratch test, the COF obtained for C3 and C4 was 0.20 and 0.15, possibly due to a higher sp^3 bonds present in this coating, which would provide higher mechanical support and, consequently, lower deformation of the system.

Results obtained for depth, area, and volume of scratch tracks are displayed in Table 6 for coatings C1, C2, C3 and C4 deposited on Cu—Be. Figs. 14 a and b display images of the depth and mean profiles of cross-sections of the scratch track. A comparison of those results indicates that the C2 showed greater track depth, area, and volume than C1. This result can also be explained by the applied bias of −50 V, which may induce the reduction of coating adhesion, as reported by Tillmann et al. [33].

In addition, wear depth and volume reductions were observed when comparing C3 and C4 coatings with C1 and C2 sample conditions. The higher mechanical support promoted by the TiN layer contributed to this behavior. Specifically, condition C4 presents an improved adhesion strength during the scratch tests than condition C3, mainly due to a thicker TiN layer. According to Conde et al. [72], considering similar composition and mechanical properties, the thicker coating would provide more resistance to wear. Conversely, contact loads in a thicker a-C coating on a soft substrate, such as Cu—Be alloy, may present inherent mechanical behavior issues. Under system deformation, the DLC film may not be able to follow the substrate deformation, which would result in cracking, delamination and surface failure, as indicated by Holmberg and Matthews [24].

4. Conclusion

In this work, two-layered coating configurations (Ti/Si/a-C and Ti/

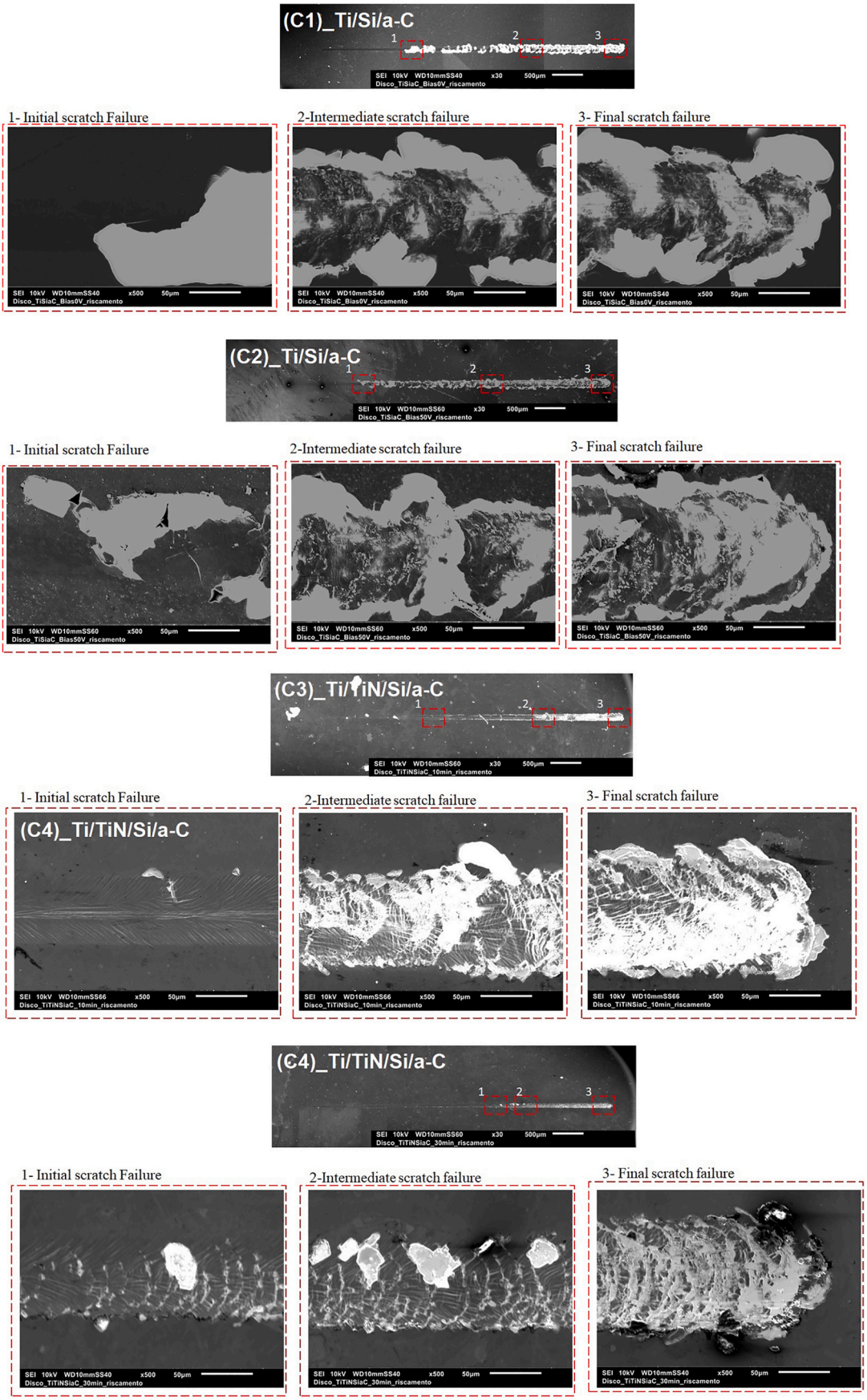

Fig. 12. Scratch track images of coated Cu-Be alloy disks and three different regions of the scratch and coating failure features are shown at higher magnifications. (a) C1; (b) C2; (c) C3 and (d) C4 conditions.

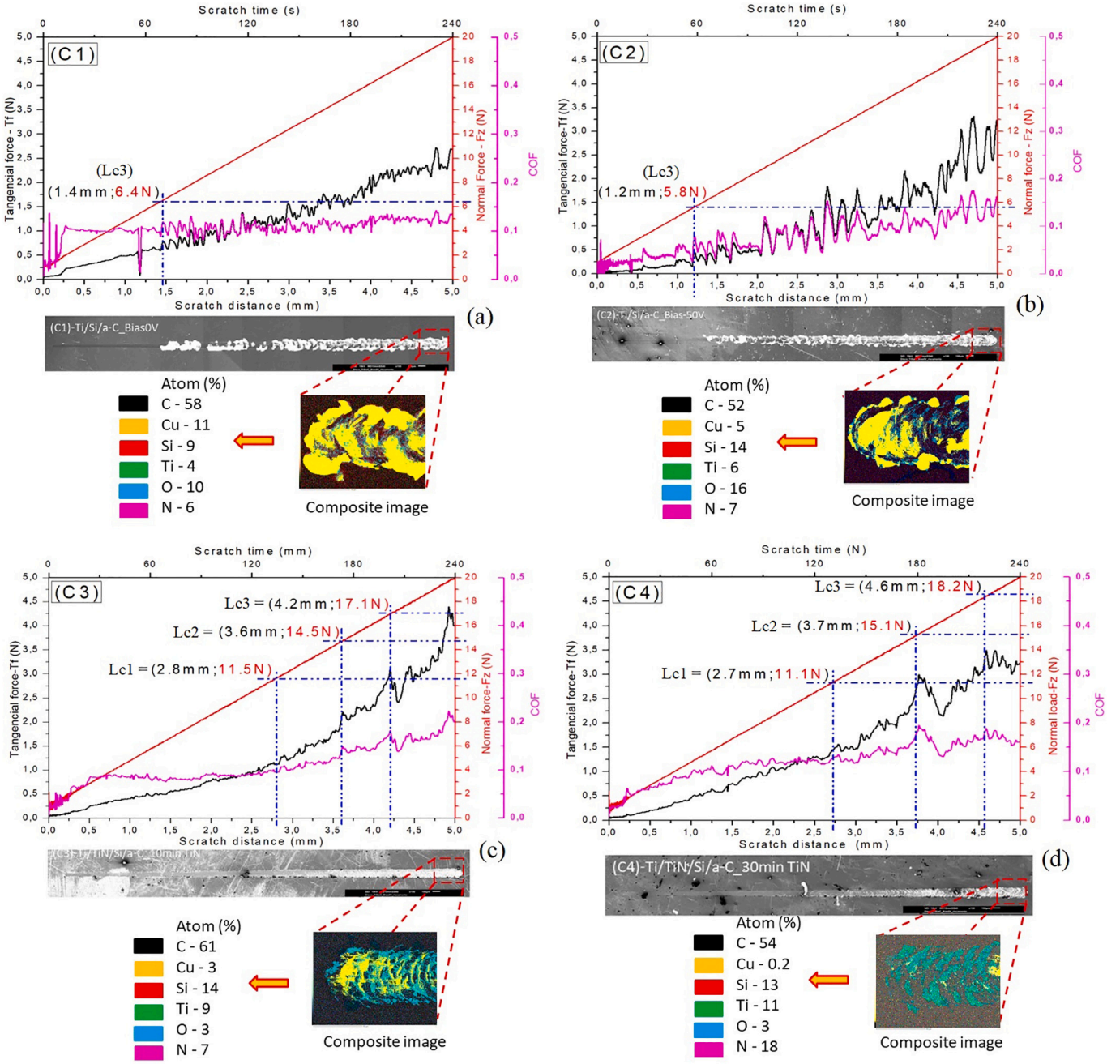

Fig. 13. Scratch curves and composite images (SEM-EDS and Image J) at the end of the scratch track for (a) C1, (b) C2, (c) C3, and (d) C4 coatings on the Cu-Be alloy surface.

Table 6
Mean depth, area, and volume of worn track obtained after scratch tests of deposited coatings on the Cu—Be alloy substrate.

Coatings	Mean depth (μm)	Area of the scratch track (μm^2)	Volume of the worn track (10^3 μm^3)
C1	2.1 ± 0.1	103 ± 4	515 ± 20
C2	2.4 ± 0.2	121 ± 5	605 ± 25
C3	1.6 ± 0.1	84 ± 3	420 ± 15
C4	1.5 ± 0.1	72 ± 2	360 ± 10

TiN/Si/a-C) were deposited using the pDCMS process. After obtaining the coatings, cross-sections, chemical analysis, surface analysis, mechanical properties and adhesion tests were carried out. The several and complementary experiments and analysis conducted allowed the conclusions as follows:

(1) The bias voltage of −50 V in condition C2 resulted in slightly lower adhesion strength and a slight increase in hardness than the 0 V bias of C1 condition. Therefore, the bias condition of the C1 was applied to C3 and C4 samples.
(2) Regarding mechanical properties, the Ti/Si/a-C coating system (C1 and C2 conditions) resulted in inferior mechanical properties and adhesion when compared to the presence of a TiN layer as in C3 and C4 conditions. The TiN layer provided improved adhesion and mechanical support to the a-C coating, resulting in a higher load caring capacity of the system.
(3) GDOES results confirmed the presence of TiN layer in both C3 and C4 conditions. Given the reduced thickness in C3 case, the TiN

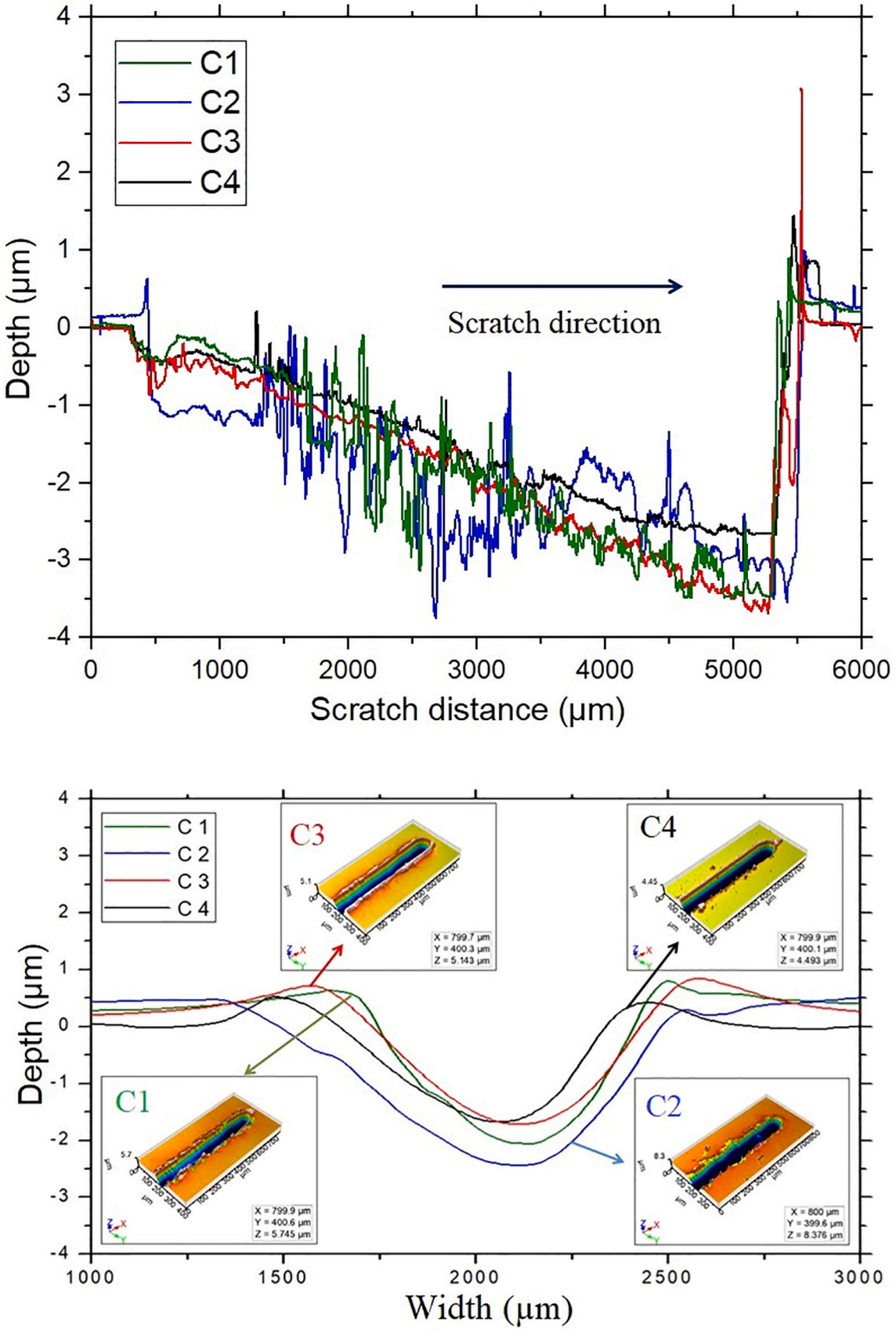

Fig. 14. Optical profilometry of scratch tracks in the coatings C1, C2, C3, and C4 deposited on Cu-Be alloy: (a) depth as a function of scratch distance (load ramp); (b) mean profile cross-section width as a function of depth. Optical 3D profilometer.

layer was only observed by glazing angle XRD in C4 coating condition.

(4) The instrumented nanoindentation tests have shown that hardness and reduced elastic modulus are superior for C3 and C4 coating conditions compared to the C1 and C2 coatings, in which a TiN interlayer was deposited between the metallic Ti and the amorphous Si layers.

(5) The greater TiN interlayer thickness in the C4 condition provided the highest critical load during the scratch test and the higher sp^3 content of the a-C layer, as observed by the Raman results, that led to a better adhesion strength and surface roughness of the designed substrate/coating system in this work.

CRediT authorship contribution statement

Conceptualization: M. D. Santos, N. K. Fukumasu, A. P. Tschiptschin, R. M. Souza, I. F. Machado.

Methodology: M. D. Santos, N. K. Fukumasu, I. F. Machado.

Investigation: N. K. Fukumasu, A. P. Tschiptschin, N.B. Lima, C. A. Figueroa, J. S. Weber, R. M. Souza, I. F. Machado.

Discussion of results: M. D. Santos, N. K. Fukumasu, A. P. Tschiptschin, N.B. Lima, C. A. Figueroa, R. M. Souza, I. F. Machado.

Writing – Original draft: M. D. Santos.

Writing – review and editing: M. D. Santos, N. K. Fukumasu, A. P. Tschiptschin, N.B. Lima, C. A. Figueroa, R. M. Souza, I. F. Machado.

Approval of the final text: M. D. Santos, N. K. Fukumasu A. P. Tschiptschin, N.B. Lima, C. A. Figueroa, J. S. Weber, R. M. Souza, I. F. Machado.

Declaration of competing interest

The authors declare no conflict of interests, personal or financial, could influence the results reported in this work.

Acknowledgements

The authors recognize the National Council for Scientific and Technological Development (CNPq), the Coordination for the Improvement of Higher Education Personnel (CAPES), the São Paulo Research Foundation (FAPESP), and the National Bank for Economic and Social Development (BNDES) for financial support. Furthermore, we recognize the support by Anton Paar from Brazil for roughness measurements in AFM tosca 400.

References

[1] V.F.C. Sousa, J. Castanheira, F.J.G. Silva, J.S. Fecheira, G. Pinto, A. Baptista, Wear behavior of uncoated and coated tools in milling operations of ampco (Cu-be) alloy, Appl. Sci. 11 (2021) 1–22, https://doi.org/10.3390/app11167762.

[2] J.R. Davis, ASM Specialty Handbook: Copper And Copper Alloys, First, ASM International Handbook Committee, Chagrin Falls, Ohio, 2001.

[3] F.L. Amorim, W.L. Weingaertner, Die-sinking electrical discharge machining of a high-strength copper-based alloy for injection molds, J. Braz.Soc. Mech. Sci. Eng. 26 (2004) 137–144, https://doi.org/10.1590/S1678-58782004000200004.

[4] M.F. Yan, Y.D. Zhu, C.S. Zhang, Y.X. Zhang, Y.X. Wang, L. Yang, Microstructure and mechanical properties of copper-titanium-nitrogen multiphase layers produced by a duplex treatment on C17200 copper-beryllium alloy, Mater. Des. 84 (2015) 10–17, https://doi.org/10.1016/j.matdes.2015.06.130.

[5] M.P. Ahmed, H.S. Jailani, Enhancing wear resistance of cryo treated Cu-Be2 alloy, SILICON 11 (2019) 105–115, https://doi.org/10.1007/s12633-018-9835-y.

[6] V. Seriacopi, E.F. Prados, N.K. Fukumasu, R.M. Souza, I.F. Machado, Mechanical behavior and abrasive mechanism mapping applied to micro-scratch tests on homogeneous and heterogeneous materials: FEM and experimental analyses, Wear 450–451 (2020) 1–15, https://doi.org/10.1016/j.wear.2020.203240.

[7] L. Yang, F.Y. Zhang, M.F. Yan, M.L. Zhang, Microstructure and mechanical properties of multiphase layer formed during thermo-diffusing of titanium into the surface of C17200 copper-beryllium alloy, Appl. Surf. Sci. 292 (2014) 225–230, https://doi.org/10.1016/j.apsusc.2013.11.121.

[8] L. Liu, H.H. Shen, X.Z. Liu, Q. Guo, T.X. Meng, Z.X. Wang, X.P. Liu, Wear resistance of TiN(Ti2N)/Ti composite layer formed on C17200 alloy by plasma surface Ti-alloying and nitriding, Appl. Surf. Sci. 26 (2016) 2605–2612, https://doi.org/10.1016/j.apsusc.2016.03.059.

[9] Y.D. Zhu, M.F. Yan, Y.X. Zhang, C.S. Zhang, Surface modification of C17200 copper-beryllium alloy by plasma nitriding of Cu-Ti gradient film, J. Mater. Eng. Perform. 27 (2018) 961–969, https://doi.org/10.1007/s11665-018-3190-4.

[10] M. Yatsuzuka, Y. Oka, M. Nishijima, K. Hiraga, Microstructure of interface for high-adhesion DLC film on metal substrates by plasma-based ion implantation, Vacuum (2008), https://doi.org/10.1016/j.vacuum.2008.03.021.

[11] A. Tyagi, R.S. Walia, Q. Murtaza, S.M. Pandey, P.K. Tyagi, B. Bajaj, A critical review of diamond like carbon coating for wear resistance applications, Int. J. Refract. Met. 78 (2019) 107–122, https://doi.org/10.1016/j.ijrmhm.2018.09.006.

[12] Y. Oka, M. Nishijima, K. Hiraga, M. Yatsuzuka, Effect of ion implantation layer on adhesion of DLC film by plasma-based ion implantation and deposition, Surf. Coat. Technol. 201 (2007) 6647–6650, https://doi.org/10.1016/j.surfcoat.2006.09.027.

[13] M.M. Morshed, D.C. Cameron, B.P. McNammara, M.S.J. Hashimi, Pre-treatment of substrates for improved adhesion of diamond-like carbon films on surgically implantable metals deposited by saddle field neutral beam source, Surf. Coat. Technol. 174–175 (2003) 579–583, https://doi.org/10.1016/S0257-8972.

[14] I. Lomakin, M. Castillo-rodríguez, X. Sauvage, Microstructure, mechanical properties and aging behaviour of nanocrystalline copper – beryllium alloy, Mater. Sci. Eng. A 744 (2019) 206–214, https://doi.org/10.1016/j.msea.2018.12.011.

[15] J. Vetter, 60years of DLC coatings: historical highlights and technical review of cathodic arc processes to synthesize various DLC types, and their evolution for industrial applications, Surf. Coat.Technol. 257 (2014) 213–240, https://doi.org/10.1016/j.surfcoat.2014.08.017.

[16] C.A. Charitidis, Nanomechanical and nanotribological properties of carbon-based thin films: a review, Int. J. Refract. Met. Hard Mater. 28 (2010) 51–70, https://doi.org/10.1016/j.ijrmhm.2009.08.003.

[17] L. Hongxi, J. Yehua, Z. Rong, T. Baoyin, Wear behaviour and rolling contact fatigue life of Ti/TiN/DLC multilayer films fabricated on bearing steel by PIIID, Vacuum 86 (2012) 848–853, https://doi.org/10.1016/j.vacuum.2011.02.015.

[18] L. Wang, S. Wan, S.C. Wang, R.J.K. Wood, Q.J. Xue, Gradient DLC-based nanocomposite coatings as a solution to improve tribological performance of aluminum alloy, Tribol. Lett. 38 (2010) 155–160, https://doi.org/10.1007/s11249-010-9585-5.

[19] A.A. Voevodin, J.M. Schneider, C. Rebholz, A. Matthews, Multilayer composite ceramic-metal-DLC coatings for sliding wear applications, Tribol. Int. 29 (1996) 559–570, https://doi.org/10.1016/0301-679X(95)00121-J.

[20] H. Maruno, A. Nishimoto, Adhesion and durability of multi-interlayered diamond-like carbon films deposited on aluminum alloy, Surf. Coat.Technol. 354 (2018) 134–144, https://doi.org/10.1016/j.surfcoat.2018.08.094.

[21] Y. Lu, G. Huang, L. Xi, Tribological and mechanical properties of the multi-layer DLC film on the soft copper substrate, Diam. Relat. Mater. 94 (2019) 21–27, https://doi.org/10.1016/j.diamond.2019.02.019.

[22] M. Khadem, O.V. Penkov, H.K. Yang, D.E. Kim, Tribology of multilayer coatings for wear reduction: a review, Friction 5 (2017) 248–262, https://doi.org/10.1007/s40544-017-0181-7.

[23] S. Flege, R. Hatada, W. Ensinger, K. Baba, Improved adhesion of DLC films on copper substrates by preimplantation, Surf. Coat.Technol. 256 (2014) 37–40, https://doi.org/10.1016/j.surfcoat.2013.12.020.

[24] K. Holmberg, A. Matthews, Coatings Tribology: Properties, Mechanisms, Deposition Techniques And Applications in Surface Engineering, Second ed., Elsevier, 2009.

[25] A. Erdemir, C. Donnet, Tribology of diamond-like carbon films: recent progress and future prospects, J. Phys. D. Appl. Phys. 39 (2006), https://doi.org/10.1088/0022-3727/39/18/R01.

[26] N.K. Fukumasu, C.F. Bernardes, M.A. Ramirez, V.J. Trava-airoldi, R.M. Souza, I. F. Machado, Local transformation of amorphous hydrogenated carbon coating induced by high contact pressure, Tribiol.Int. 124 (2018) 200–208, https://doi.org/10.1016/j.triboint.2018.04.006.

[27] T.W. Scharf, S.V. Prasad, Solid lubricants: a review, J. Mater. Sci. 48 (2013) 511–531, https://doi.org/10.1007/s10853-012-7038-2.

[28] S.A. Catledge, Y.K. Vohra, D.D. Jackson, S.T. Weir, Adhesion of nanostructured diamond film on a copper-beryllium alloy, J. Mater. Res. 23 (2008) 2373–2381, https://doi.org/10.1557/jmr.2008.0287.

[29] L.V.C. Assali, W.V.M. Machado, J.F. Justo, Titanium impurities in silicon, diamond, and silicon carbide, <sb:contribution><sb:title>Braz.</sb:title> </sb:contribution><sb:host><sb:issue><sb:series><sb:title>J. Phys.</sb:title></sb:series></sb:issue></sb:host> 34 (2004) 602–604, https://doi.org/10.1590/S0103-97332004000400016.

[30] Q.H. Fan, A. Fernandes, E. Pereira, J. Grácio, Adherent diamond coating on copper using an interlayer, Vacuum 52 (1999) 193–198, https://doi.org/10.1016/s0042-207x(98)00212-7.

[31] K. Honjo, S. Akio, Influence of carbide formation on the strength of carbon fibres on which silicon and titanium have been deposited, J.Mater. Sci. 21 (1986) 2043–2048, https://doi.org/10.1007/BF00547945.

[32] S. Neuville, A. Matthews, A perspective on the optimisation of hard carbon and related coatings for engineering applications, Thin Solid Films 515 (2007) 6619–6653, https://doi.org/10.1016/j.tsf.2007.02.011.

[33] W. Tillmann, N.F. Lopes Dias, D. Stangier, M. Bayer, H. Moldenhauer, J. Debus, M. Schmitz, U. Berges, C. Westphal, Interaction effects of cathode power, bias voltage, and mid-frequency on the structural and mechanical properties of sputtered amorphous carbon films, Appl. Surf. Sci. 487 (2019) 857–867, https://doi.org/10.1016/j.apsusc.2019.05.131.

[34] J. Filik, P.W. May, S.R.J. Pearce, R.K. Wild, K.R. Hallam, in: XPS and laser Raman analysis of hydrogenated amorphous carbon films 12, 2003, pp. 974–978, https://doi.org/10.1016/S0925-9635(02)00374-6.

[35] S. Nakao, J. Choi, J. Kim, S. Miyagawa, Y. Miyagawa, M. Ikeyama, in: Effects of positively and negatively pulsed voltages on the microstructure of DLC films prepared by bipolar-type plasma based ion implantation 15, 2006, pp. 884–887, https://doi.org/10.1016/j.diamond.2005.10.032.
[36] F.C. Tai, S.C. Lee, J. Chen, C. Wei, S.H. Chang, in: Multipeak fitting analysis of Raman spectra on DLCH film 2009, 2009, pp. 1055–1059, https://doi.org/10.1002/jrs.2234.
[37] L. Liu, Z. Wu, X. An, S. Xiao, S. Cui, H. Lin, R.K.Y. Fu, X. Tian, R. Wei, P.K. Chu, F. Pan, Excellent adhered thick diamond-like carbon coatings by optimizing hetero-interfaces with sequential highly energetic Cr and C ion treatment, J. Alloys Compd. 735 (2018) 155–162, https://doi.org/10.1016/j.jallcom.2017.11.057.
[38] Y.M. Wu, J.Q. Liu, H.T. Cao, Z.Y. Wu, Q. Wang, Y.P. Ma, H. Jiang, F. Wen, Y.T. Pei, On the adhesion and wear resistance of DLC films deposited on nitrile butadiene rubber: a Ti-C interlayer, Diam. Relat. Mater. 101 (2020), https://doi.org/10.1016/j.diamond.2019.107563.
[39] A. Ferrari, J. Robertson, Interpretation of Raman spectra of disordered and amorphous carbon, Phys. Rev. BCondens. Matter Mater. Phys. 61 (2000) 14095–14107, https://doi.org/10.1103/PhysRevB.61.14095.
[40] ISO 14577-4:2007(E), Metallic Materials - Instrumented Indentation Test for Hardness And Materials Parameters - Part 4: Test Method for Metallic And Non-metallic Coatings, 2007. Geneva, Switzerland.
[41] I.F. Machado, G. Boidi, N.K. Fukumasu, A.J.O. Tertuliano, V. Seriacopi, R. M. Souza, Effect of sintering densification on micro-scale mechanical and tribological behaviour of niobium carbide, Wear 482–483 (2021), 203958, https://doi.org/10.1016/j.wear.2021.203958.
[42] W.C. Oliver, G.M. Pharr, An improved technique for determining hardness and elastic modulus using load and displacement sensing indentation experiments, J. Mater. Res. 7 (1992) 1564–1583, https://doi.org/10.1557/JMR.1992.1564.
[43] ASTM International C1624 - 05, Standard Test Method for Adhesion Strength And Mechanical Failure Modes of Ceramic Coatings by Quantitative Single Point Scratch Testing, West Conshohocken, PA, USA, 2005, https://doi.org/10.1520/C1624-05.
[44] Y. Wang, L. Wang, G. Zhang, S.C. Wang, R.J.K. Wood, Q. Xue, Effect of bias voltage on microstructure and properties of Ti-doped graphite-like carbon films synthesized by magnetron sputtering, Surf. Coat.Technol. 205 (2010) 793–800, https://doi.org/10.1016/j.surfcoat.2010.07.112.
[45] Y. Wang, H. Li, L. Ji, F. Zhao, Q. Kong, Y. Wang, X. Liu, W. Quan, H. Zhou, J. Chen, Microstructure, mechanical and tribological properties of graphite-like amorphous carbon films prepared by unbalanced magnetron sputtering, Surf. Coat.Technol. 205 (2011) 3058–3065, https://doi.org/10.1016/j.surfcoat.2010.11.019.
[46] J. Chen, Y. Wang, H. Li, L. Ji, Y. Wu, Y. Lv, X. Liu, Y. Fu, H. Zhou, Microstructure, morphology and properties of titanium containing graphite-like carbon films deposited by unbalanced magnetron sputtering, Tribol. Lett. 49 (2013) 47–59, https://doi.org/10.1007/s11249-012-0041-6.
[47] K.P. Shaha, Y.T. Pei, D. Martinez-Martinez, J.C. Sanchez-Lopez, J.T.M. De Hosson, Effect of process parameters on mechanical and tribological performance of pulsed-DC sputtered TiC/a-C: H nanocomposite films, Surf. Coat.Technol. 205 (2010) 2633–2642, https://doi.org/10.1016/j.surfcoat.2010.10.020.
[48] J.A. Thornton, Influence of apparatus geometry and deposition conditions on the structure and topography of thick sputtered coatings, J. Vac. Sci. Technol. 11 (1974) 666–670, https://doi.org/10.1116/1.1312732.
[49] I. Petrov, P.B. Barna, L. Hultman, J.E. Greene, Microstructural evolution during film growth, J. Vac. Sci. Technol. A VacuumSurf.Films 21 (2003) S117–S128, https://doi.org/10.1116/1.1601610.
[50] J. Jiang, R.D. Arnell, The effect of substrate surface roughness on the wear of DLC coatings, Wear 239 (2000) 1–9, https://doi.org/10.1016/S0043-1648(99)00351-8.
[51] F. Svahn, Å. Kassman-Rudolphi, E. Wallén, The influence of surface roughness on friction and wear of machine element coatings, Wear 254 (2003) 1092–1098, https://doi.org/10.1016/S0043-1648(03)00341-7.
[52] C.F. Bernardes, N.K. Fukumasu, A.O. Lima, R.M. Souza, I.F. Machado, Influence of growth defects on the running-in behavior of an a-C:H: W coating under pure sliding contact conditions, Surf. Coat.Technol. 402 (2020), 126278, https://doi.org/10.1016/j.surfcoat.2020.126278.
[53] D. Hofmann, S. Kunkel, K. Bewilogua, R. Wittorf, From DLC to Si-DLC based layer systems with optimized properties for tribological applications, Surf. Coat.Technol. 215 (2013) 357–363, https://doi.org/10.1016/j.surfcoat.2012.06.094.
[54] W. Tillmann, N.F. Lopes Dias, C. Franke, D. Kokalj, D. Stangier, C.A. Thomann, J. Debus, Mechanical properties and adhesion behavior of amorphous carbon films with bias voltage controlled TixCy interlayers on Ti6Al4V, Diam. Relat. Mater. 115 (2021), https://doi.org/10.1016/j.diamond.2021.108361.
[55] O. Kluth, G. Schöpe, J. Hüpkes, C. Agashe, J. Müller, B. Rech, Modified Thornton model for magnetron sputtered zinc oxide: film structure and etching behaviour, Thin Solid Films 442 (2003) 80–85, https://doi.org/10.1016/S0040-6090(03)00949-0.
[56] J.A. Thornton, High rate thick film growth, Annu. Rev. Mater. Sci. 7 (1977) 239–260, https://doi.org/10.1146/annurev.ms.07.080177.001323.
[57] P. Saikia, A. Joseph, R. Rane, B. Saikia, S. Mukherjee, Role of substrate and deposition conditions on the texture evolution of titanium nitride thin film on bare and plasma-nitrided high-speed steel, J. Theor. Appl. Phys. 7 (2013) 66, https://doi.org/10.1186/2251-7235-7-66.
[58] B.D. Cullity, X-ray Diffraction, Addison - Wesley publishing company Inc, Notre Dame, Indiana, 1959.
[59] K. Shimizu, H. Habazaki, P. Skeldon, G.E. Thompson, R.K. Marcus, Influence of interracial depth on depth resolution during GDOES depth profiling analysis of thin alumina films, Surf. Interface Anal. 31 (2001) 869–873, https://doi.org/10.1002/sia.1120.
[60] C. Florian, R. Wonneberger, A. Undisz, S.V. Kirner, K. Wasmuth, D. Spaltmann, J. Krüger, J. Bonse, Chemical effects during the formation of various types of femtosecond laser-generated surface structures on titanium alloy, Appl. Phys. A 126 (2020) 266, https://doi.org/10.1007/s00339-020-3434-7.
[61] M. Huang, X. Zhang, P. Ke, A. Wang, Graphite-like carbon films by high power impulse magnetron sputtering, Appl. Surf. Sci. 283 (2013) 321–326, https://doi.org/10.1016/j.apsusc.2013.06.109.
[62] A.C. Ferrari, Determination of bonding in diamond-like carbon by Raman spectroscopy, Diam. Relat. Mater. 11 (2000) 1053–1061, https://doi.org/10.1016/S0925-9635(01)00730-0.
[63] Z.Y. Song, Q.Y. Sun, L. Xiao, L. Liu, H. Wang, W. Chen, J. Sun, P. Ge, The influence of prior cold deformation on precipitation of alpha phase and variation of hardness in Ti-10Mo-8V-1Fe-3.5Al during aging treatment, J. Mater. Res. 24 (2009) 452–458, https://doi.org/10.1557/JMR.2009.0051.
[64] F.J. Valencia, J. Santiago, R.I. González, R. González-Arrabal, C. Ruestes, M. Perez Díaz, M.A. Monclus, J. Molina-Aldareguia, P.D. Nuñez, F. Munoz, M. Kiwi, J. M. Perlado, E.M. Bringa, Nanoindentation of amorphous carbon: a combined experimental and simulation approach, Acta Mater. 203 (2021), https://doi.org/10.1016/j.actamat.2020.116485.
[65] V. Kulikovsky, P. Bohac, F. Franc, A. Deineka, V. Vorlicek, L. Jastrabik, Hardness, intrinsic stress, and structure of the a-C and a-C: H films prepared by magnetron sputtering, Diam. Relat. Mater. 10 (2001) 1076–1081, https://doi.org/10.1016/S0925-9635(00)00525-2.
[66] D. Martínez-Martínez, C. López-Cartes, A. Fernández, J.C. Sánchez-López, Influence of the microstructure on the mechanical and tribological behavior of TiC/a-C nanocomposite coatings, Thin Solid Films 517 (2009) 1662–1671, https://doi.org/10.1016/j.tsf.2008.09.091.
[67] A. Leyland, A. Matthews, On the significance of the H/E ratio in wear control: a nanocomposite coating approach to optimised tribological behaviour, Wear 246 (2000) 1–11, https://doi.org/10.1016/S0043-1648(00)00488-9.
[68] S.J. Bull, Failure mode maps in the thin scratch adhesion test, Tribiol.Int. 30 (1997) 491–498, https://doi.org/10.1016/S0301-679X(97)00012-1.
[69] W. Tillmann, E. Vogli, F. Hoffmann, P. Kemdem, Influence of substrate nitriding on adhesion, friction and wear resistance of DLC (diamond-like carbon)-coatings, Key Eng. Mater. 438 (2010) 211–218, https://doi.org/10.4028/www.scientific.net/KEM.438.211.
[70] V. Godinho, C. Fernández-Ramos, D. Martinez-Martinez, J. García-Lopes, J. C. Sánchez-López, A. Fernández, Microstructural and chemical characterisation techniques for nanostructured and amorphous coatings, Eur. Phys. J. 43 (2008) 333–341, https://doi.org/10.1051/epjap.
[71] D.G. Liu, J.P. Tu, C.F. Hong, C.D. Gu, Y.J. Mai, R. Chen, Improving mechanical properties of a-CNx films by Ti_TiN_CNx gradient multilayer, Appl. Surf. Sci. 257 (2010) 487–494, https://doi.org/10.1016/j.apsusc.2010.07.018.
[72] F.F. Conde, J.A.A. Diaz, G.F. Da Silva, A.P. Tschiptschin, Dependence of wear and mechanical behavior of nitrocarburized/CrN/Dlc layer on film thickness, Mater. Res. 22 (2019) 1–10, https://doi.org/10.1590/1980-5373-MR-2018-0499.